Author/s:
Short, E;Lane, TP;Bishop, CH;Wheeler, MC

Title:
Diurnally Forced Tropical Gravity Waves under Varying Stability

Date:
2023-10-01

Citation:
Short, E., Lane, T. P., Bishop, C. H. & Wheeler, M. C. (2023). Diurnally Forced Tropical Gravity Waves under Varying Stability. Journal of the Atmospheric Sciences, 80 (10), pp.2557-2579. https://doi.org/10.1175/JAS-D-23-0074.1.

Persistent Link:
https://hdl.handle.net/11343/340242

Diurnally Forced Tropical Gravity Waves Under Varying Stability

Ewan Short[a] , Todd P. Lane[a] , Craig H. Bishop[a] , Matthew C. Wheeler[b]

[a] *School of Geography, Earth & Atmospheric Sciences, and ARC Centre of Excellence for Climate Extremes, The University of Melbourne, Melbourne, Victoria, Australia.*

[b] *Bureau of Meteorology, Melbourne, Australia.*

Corresponding author: Ewan Short, shorte1@student.unimelb.edu.au

ABSTRACT: Diurnal processes play a primary role in tropical weather. A leading hypothesis is that atmospheric gravity waves diurnally forced near coastlines propagate both offshore and inland, encouraging convection as they do so. In this study we extend the linear analytic theory of diurnally forced gravity waves, allowing for discontinuities in stability, and for linear changes in stability over a finite depth "transition-layer". As an illustrative example, we first consider the response to a commonly studied heating function emulating diurnally oscillating coastal temperature gradients, with a low-level stability change between the boundary layer and troposphere. Gravity wave rays resembling the upper branches of "St. Andrew's Cross" are forced along the coastline at the surface, with the stability changes inducing reflection, refraction and ducting of the individual waves comprising the rays, with analogous behaviour evident in the rays themselves. Refraction occurs smoothly in the transition-layer solution, with substantially less reflection than in the discontinuous solution. Second, we consider a new heating function which emulates an upper-level convective heating diurnal cycle, and consider stability changes associated with the tropical tropopause. Reflection, refraction and ducting again occur, with the lower branches of St. Andrew's Cross now evident. We compare these solutions to observations taken during the Years of the Maritime Continent field campaign, noting better qualitative agreement with the transition-layer solution than the discontinuous solution, suggesting the tropopause is an even weaker gravity wave reflector than previously thought.

SIGNIFICANCE STATEMENT: This study extends our theoretical understanding of how forced atmospheric gravity waves change with atmospheric structure. Gravity wave behaviour depends on atmospheric stability: how much the atmosphere resists vertical displacements of air. Where stability changes, waves reflect and refract, analogously to when light passes from water to air. Our study presents new mathematical tools for understanding this reflection and refraction, demonstrating reflection is substantially weaker when stability increases over "transition-layers", than when stability increases suddenly. Our results suggest the tropical tropopause reflects less gravity wave energy than previously thought, with potential design implications for weather and climate models, to be assessed in future work.

1. Introduction

Diurnal processes determine much of the variability of tropical weather. For rainfall, the amplitude of the mean diurnal harmonic exceeds 70% of the seasonal mean in many coastal tropical regions (Minobe and Takebayashi 2015). In locations like the Maritime Continent and the Bight of Panama, coastal processes themselves likely induce between $40-60\%$ of rainfall (Bergemann et al. 2015). Satellite observations indicate that the peak of the rainfall diurnal harmonic occurs progressively later with distance from the coastline, in some locations propagating up to 1000 km offshore (e.g. Yang and Slingo 2001). Analogous behaviour has been observed for the diurnal cycle of winds (Gille et al. 2005), leading to many hypotheses on the interconnectedness of these processes (e.g. Mori et al. 2004; Robinson et al. 2008; Vincent and Lane 2016; Kilpatrick et al. 2017).

One theory, originating with Mapes et al. (2003), is that gravity waves forced along or near coastlines propagate both offshore and inland, destabilising the atmosphere and promoting convection as they go. These waves may be forced by topography or convective heating near coastlines, or by the diurnally oscillating temperature gradient associated with the coastline itself. In the tropics, gravity waves forced by coastal temperature gradients can be interpreted as the linear component of the land-sea breeze, manifesting as onshore surface winds in the afternoon and evening (the sea-breeze), and offshore winds in the morning (the land-breeze).

Rotunno (1983) demonstrated using a simple, 2-dimensional linear theory, that for latitudes between $\pm 30^\circ$, oscillating coastal temperature gradients force gravity wave rays, i.e. packets of

gravity waves which propagate far offshore. The rays resemble the upper half of "St Andrew's Cross", the signature of internal gravity-waves generated by oscillatory forcings (Mowbray and Rarity 1967). The differing behaviour of the land-sea breeze poleward and equatorward of 30° was subsequently corroborated by non-linear numerical simulations (Yan and Anthes 1987).

Rotunno's original theory employed the Boussinesq equations, linearised about a hydrostatic, stationary atmosphere, with a free-slip lower boundary. Subsequent studies modified his approach to incorporate momentum diffusivity (Niino 1987), friction (Dalu and Pielke 1989; Du and Rotunno 2015; Das Gupta et al. 2015), shore-parallel thermal wind shear (Drobinski et al. 2011), non-linear coastlines (Li and Chao 2016; Jiang 2012a), constant background winds (Qian et al. 2009; Du and Rotunno 2018) and background winds that shear linearly with height (Du et al. 2019). Of particular relevance to the present study is the theory of Jiang (2012b), who divided the vertical domain into at most 3 distinct layers, allowing discontinuities in the Brunt-Väisälä frequency N, potential temperature, and background winds between each layer, but requiring they be constant within each layer. To solve the resulting equations, Jiang modified the heating function introduced by Rotunno to constrain heating to lie within a single layer.

In the present study, we consider some new extensions of Rotunno's theory to situations involving non-constant stability, i.e. a non-constant Brunt-Väisälä frequency N. We first consider the case of a step change in N, i.e. $N = N_1$ below some height H_1 and $N = N_2$ above H_1, where N_1 and N_2 are distinct positive numbers. This analysis is similar to that of Lindzen and Tung (1976), who considered the analestic equations, and calculated the reflection and refraction coefficients associated with a stability discontinuity for a single gravity wave forced below the stability change. Here we consider the simpler Bousinesq equations, but the more complex case of a forced spectrum of waves, and the effect of forcing above the stability change. This analysis is also similar to that of Jiang (2012b) discussed above, although here we consider the simpler problem of resting horizontal background winds, but the more complex situation of forcing above and below the stability change, and the possibility of a stability decrease with height.

Second, we consider the case where $N = N_1$ below some height H_1, $N = N_2$ above another height H_2, with $H_2 > H_1$, and with N transitioning linearly between N_1 and N_2 between H_1 and H_2. This setup admits an analytic solution that generalises the piecewise-constant solution. To the best of our knowledge, a solution to this problem is yet to appear in the published literature, with the

closest solution being for the three layer model considered by Jiang (2012b), in which waves are forced only in the lowest vertical layer, and N is constant within each layer. We will refer to our two solutions as the "piecewise-constant" and "transition-layer" solutions respectively. We present illustrative examples of both solutions with a low level stability change emblematic of that between the boundary layer and free troposphere, as this setup is easiest to interpret and compare with previous work.

We then generalise the theory by considering an alternative heating function which emulates the upper level heating associated with a diurnally recurring convective line. This extension is straightforward, as our core mathematical results are independent of the spatial structure of the heating function. We use this extended theory to interpret soundings acquired during the Australian leg of the Years of the Maritime Continent (YMC) campaign (Yoneyama and Zhang 2020), focusing on the stability change between the troposphere and stratosphere.

The remainder of this paper is organised as follows. In sections 2 and 3 we present the piecewise-constant and transition-layer solutions respectively, and provide illustrative example solutions using the original low-level surface heating function of Rotunno (1983). In section 4 we introduce the YMC sounding data and the alternative upper-level convective diurnal heating function, and interpret the YMC data in light of the extended theory. Section 5 provides discussion and a conclusion.

2. Piecewise Constant Solution

We begin with the dimensional equations for Boussinesq, hydrostatic flow, linearised about a resting background state:

$$\frac{\partial u^*}{\partial t^*} - f v^* = -\frac{\partial p^*}{\partial x^*}, \tag{1}$$

$$\frac{\partial v^*}{\partial t^*} + f u^* = 0, \tag{2}$$

$$\frac{\partial p^*}{\partial z^*} = b^*, \tag{3}$$

$$\frac{\partial b^*}{\partial t^*} + N(z)^2 w^* = Q^*, \tag{4}$$

$$\frac{\partial u^*}{\partial x^*} + \frac{\partial w^*}{\partial z^*} = 0, \tag{5}$$

$$Q^* = \frac{Q_0}{\pi}\left(\frac{\pi}{2} + \tan^{-1}\frac{x^*}{L}\right)\exp\left(-\frac{z^*}{H}\right)\cos(\omega t^*), \tag{6}$$

$$w^*(z^* = 0) = 0, \tag{7}$$

where x^* is the shore-perpendicular direction, with $x^* < 0$ and $x^* > 0$ representing sea and land respectively. The time variable t^* denotes seconds since noon local solar time (LST). The Coriolis parameter $f = 2\omega \sin\phi$ is assumed constant, ω the angular frequency of the earth and ϕ the latitude, with $|\phi| < 30°$. The functions u^*, v^*, w^* are the velocity perturbations, p^* is the Bousinesq disturbance pressure, and $b^* = g\frac{\theta'}{\theta_0}$ is the buoyancy, where g is gravity, and θ_0 and θ' are the surface and deviation potential temperatures respectively. The function Q^* represents the coastal heating cycle, with L the coastal width, Q_0 the heating amplitude, and H the vertical scale of the heating. As discussed by Rotunno (1983), this function parametrizes surface solar heating, and the turbulent diffusion of thermal energy through the lower atmosphere, idealising this diffusion as instantaneous. Figure 1 illustrates Q^* for $Q_0 = 1.2 \times 10^{-5}\,\mathrm{m\,s^{-3}}$, $L = 50\,\mathrm{km}$ and $H = 1\,\mathrm{km}$.

Gravity wave solutions to equations 1 - 7 are, strictly speaking, two-dimensional linear Boussinesq hydrostatic internal gravity waves; we will subsequently refer to these simply as "waves". Equations 1 - 7 are identical to those considered by Rotunno (1983), except we no longer assume N is constant. Instead, we take

$$N(z) = \begin{cases} N_1 & 0 \le z^* \le H_1, \\ N_2 & z^* > H_1, \end{cases} \tag{8}$$

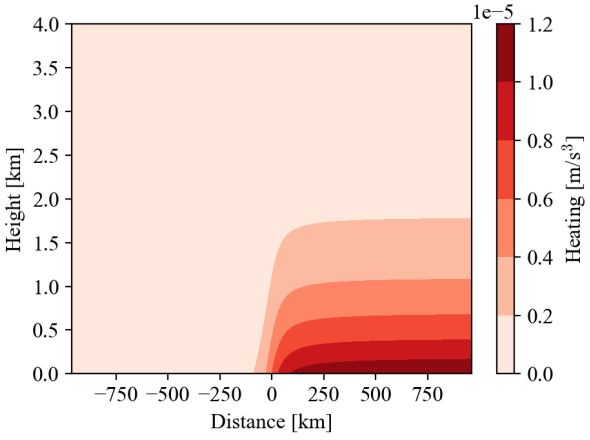

FIG. 1. The heating function given by equation 6 at noon LST, i.e. $t^* = 0$, with $L = 50\,\text{km}$, $H = 1\,\text{km}$ and $Q_0 = 1.2\times10^{-5}\,\text{m}\,\text{s}^{-3}$.

where N_1 and N_2 are positive constants, and $H_1 > 0$. Following Qian et al. (2009), we define the non-dimensional variables

$$\begin{aligned} x^* &= \frac{N_1 H}{\omega}x, \quad y^* = \frac{N_1 H}{\omega}y, \quad z^* = Hz, \quad t^* = \frac{t}{\omega}, \\ Q^* &= Q_0 Q, \quad u^* = \frac{Q_0}{N_1\omega}u, \quad v^* = \frac{Q_0}{N_1\omega}v, \quad w^* = \frac{Q_0}{N_1^2}w, \\ b^* &= \frac{Q_0}{\omega}b, \quad p^* = \frac{Q_0 H}{\omega}p, \end{aligned} \tag{9}$$

noting $t = 2\pi$ corresponds to $t^* = 1$ day in dimensional coordinates. Substituting, we obtain a set of dimensionless equations,

$$u_t - \frac{f}{\omega}v = -p_x, \tag{10}$$

$$v_t + \frac{f}{\omega}u = 0, \tag{11}$$

$$p_z = b, \tag{12}$$

$$u_x + w_z = 0, \tag{13}$$

$$b_t + n(z)^2 w = Q, \tag{14}$$

$$Q = \frac{1}{\pi}\left(\frac{\pi}{2} + \tan^{-1}\frac{x}{\mathcal{L}}\right)\exp(-z)\cos(t), \tag{15}$$

$$w(z=0) = 0, \tag{16}$$

where $\mathcal{L} = \frac{\omega L}{N_1 H}$ is the non-dimensional coastal width. We define additional non-dimensional parameters $\mathcal{H}_1 = \frac{H_1}{H}$ and $\mathcal{N} = \frac{N_2}{N_1}$, where $\mathcal{N} \neq 1$, and the vertical subdomains $D_1 = [0, \mathcal{H}_1]$ and $D_2 = (\mathcal{H}_1, \infty)$. The function $n(z)$ is then given by

$$n(z) = \begin{cases} 1 & z \in D_1, \\ \mathcal{N} & z \in D_2. \end{cases} \tag{17}$$

Defining the stream function ψ by $(u, w) = (\psi_z, -\psi_x)$, equations 10 - 16 can be combined to yield

$$\psi_{zztt} + \frac{f^2}{\omega^2}\psi_{zz} + n(z)^2\psi_{xx} = -Q_x. \tag{18}$$

Taking the Fourier transform with respect to x of both sides of equation 18 gives

$$\tilde{\psi}_{zztt} + \frac{f^2}{\omega^2}\tilde{\psi}_{zz} - \kappa^2 n(z)^2\tilde{\psi} = -e^{-\mathcal{L}|\kappa|}e^{-z}\frac{e^{it} + e^{-it}}{2}, \tag{19}$$

where $\tilde{\psi}(\kappa, z, t) = \mathcal{F}(\psi(x, z, t)) = \int_{-\infty}^{\infty} \psi e^{-i\kappa x}\, dx$ is the Fourier transform of ψ. As noted by Qian et al. (2009), the inverse Fourier transform can be calculated as

$$\psi = \mathcal{F}^{-1}\left(\tilde{\psi}(\kappa, z, t)\right) = \mathrm{Re}\left\{\frac{1}{\pi}\int_0^{\infty} \tilde{\psi}(\kappa, z, t)e^{i\kappa x}\, d\kappa\right\}, \tag{20}$$

so we can assume without loss of generality $\kappa > 0$ in equation 19. Linear independence of e^{it} and e^{-it} implies we may express $\tilde{\psi}(\kappa, z, t) = \hat{\psi}_1(\kappa, z)e^{it} + \hat{\psi}_2(\kappa, z)e^{-it}$ and solve for $\hat{\psi}_1$ and $\hat{\psi}_2$ separately, which, as noted by Qian et al. (2009), contribute the left-ward and right-ward propagating components of ψ respectively. The perturbation velocities u and w are then

$$u = \mathcal{F}^{-1}\left(\frac{\partial\tilde{\psi}}{\partial z}\right), \tag{21}$$

$$w = \mathcal{F}^{-1}\left(i\kappa\tilde{\psi}\right). \tag{22}$$

Consider first the positive mode $\hat{\psi}_1$, dropping the subscript while the context is clear. Equation 19 reduces to

$$\hat{\psi}_{zz} + m^2 n(z)^2 \hat{\psi} = \frac{1}{2\mathcal{A}^2} e^{-\mathcal{L}\kappa} e^{-z}, \tag{23}$$

where we have defined the non-dimensional number $\mathcal{A} = \sqrt{1 - \frac{f^2}{\omega^2}}$, which is real for latitudes between $\pm 30°$, and $m = \frac{\kappa}{\mathcal{A}} > 0$, which is the non-dimensional vertical wavenumber for $z \in D_1$, noting the corresponding dimensional vertical wavenumber is $m^* = \frac{m}{H}$. As discussed by Rotunno (1983), $\mathcal{A}$ determines the aspect ratio of the non-dimensional solution, which becomes unphysical as $f \to \omega$ due to the absence of friction from the theory. As noted by Jiang (2012b), conservation of mass requires continuity of w, and therefore of $\hat{\psi}$, at $\mathcal{H}_1$. Furthermore, as noted by Lindzen and Tung (1976), integrating equation 23 over the interval $(\mathcal{H}_1 - \epsilon, \mathcal{H}_1 + \epsilon)$, and taking the limit as $\epsilon \to 0$, we obtain the condition that $\hat{\psi}_z$, and therefore u, must also be continuous at $\mathcal{H}_1$. Note the above reductions and matching conditions also apply to $\hat{\psi}_2$.

Before solving equation 23, consider first its unforced analogue,

$$\hat{\psi}_{zz} + m^2 n(z)^2 \hat{\psi} = 0. \tag{24}$$

This reduces to a pair of wave equations for $z \in D_1$ and $z \in D_2$. The general solutions to these equations are given by linear combinations of $e^{im(z-\mathcal{H}_1)}$ and $e^{-im(z-\mathcal{H}_1)}$ for $z \in D_1$, and linear combinations of $e^{im\mathcal{N}(z-\mathcal{H}_1)}$ and $e^{-im\mathcal{N}(z-\mathcal{H}_1)}$ for $z \in D_2$. To develop physical intuition, we first consider two simpler sub-problems.

First, ignore the lower boundary, but apply the matching conditions at $\mathcal{H}_1$, and the radiation condition above $\mathcal{H}_1$. Recall that gravity waves propagate energy at the group velocity, the vertical component of which is negative that of the phase velocity. Thus for the positive mode e^{it}, the radiation condition requires we select only the $e^{im\mathcal{N}(z-\mathcal{H}_1)}$ mode above $\mathcal{H}_1$. The general solution thus reduces to

$$\hat{\psi} = \begin{cases} C\frac{\mathcal{N}+1}{2} e^{im(z-\mathcal{H}_1)} + C\frac{1-\mathcal{N}}{2} e^{-im(z-\mathcal{H}_1)} & z \in D_1, \\ C e^{im\mathcal{N}(z-\mathcal{H}_1)} & z \in D_2, \end{cases} \tag{25}$$

where $C \in \mathbb{C}$ is an unknown constant. This solution represents a wave propagating energy upward, that is partially reflected and partially refracted at $\mathcal{H}_1$. By taking ratios of amplitudes, we can define the reflection and refraction coefficients

$$r_1 = \left| \frac{1-\mathcal{N}}{1+\mathcal{N}} \right|, \tag{26}$$

$$r_2 = \frac{2}{\mathcal{N}+1}, \tag{27}$$

respectively, which are special cases of those derived by Lindzen and Tung (1976). As $\mathcal{N} \to \infty$, there is perfect reflection, and no refraction, with $z = \mathcal{H}_1$ acting like a rigid upper boundary. As $\mathcal{N} \to 0$, we also approach perfect reflection, but the incident and reflected waves are now in phase at $\mathcal{H}_1$, implying the amplitude of the refracted wave must be twice that of the incident wave.

Second, suppose we solve equation 24 again, reintroducing the rigid lower boundary at $z = 0$, but not applying the radiation condition. We again apply the matching conditions at $\mathcal{H}_1$. The general solution is now

$$\hat{\psi} = \begin{cases} \frac{B}{2i} e^{imz} - \frac{B}{2i} e^{-imz} & z \in D_1, \\ \frac{B}{2i\mathcal{N}} R e^{im\mathcal{N}(z-\mathcal{H}_1)} - \frac{B}{2i\mathcal{N}} \bar{R} e^{-im\mathcal{N}(z-\mathcal{H}_1)} & z \in D_2 \end{cases} \tag{28}$$

where $B \in \mathbb{C}$ is an unknown constant, and $R = \cos(m\mathcal{H}_1) + i\mathcal{N}\sin(m\mathcal{H}_1)$, with $\bar{R}$ the complex conjugate of R. By writing R in complex polar-form, equation 28 may also be expressed,

$$\hat{\psi} = \begin{cases} B\sin(mz) & z \in D_1, \\ \frac{B\sqrt{\cos^2(m\mathcal{H}_1) + \mathcal{N}^2\sin^2(m\mathcal{H}_1)}}{\mathcal{N}} \sin\left[m\mathcal{N}(z-\mathcal{H}_1) + \mathrm{Arg}\,(R)\right] & z \in D_2, \end{cases} \tag{29}$$

where $\mathrm{Arg}\,(R)$ denotes the complex argument of R. Equation 28 describes the vertical structure of the wave that results from the interference of the upward and downward propagating disturbances, noting the resulting structure does not propagate in the vertical. We define the "ducting coefficient" r_3 by taking the ratio of the amplitudes of the waves in D_1 and D_2:

$$r_3 = \frac{\mathcal{N}}{\sqrt{\cos^2(m\mathcal{H}_1) + \mathcal{N}^2\sin^2(m\mathcal{H}_1)}}. \tag{30}$$

It follows that r_3 has stationary points when $m\mathcal{H}_1 = \frac{\pi(2k-1)}{2}$ and $m\mathcal{H}_1 = \pi k$, where k is a natural number, from which resonance conditions can be inferred. Note that as $\mathcal{N} \to 0$, $r_3 \to 0$, and $z = \mathcal{H}_1$ behaves like a rigid lower boundary. As $\mathcal{N} \to \infty$, $r_3 \to \left|\frac{1}{\sin(m\mathcal{H}_1)}\right|$, noting $r_3 \to \infty$ as $m\mathcal{H}_1 \to k\pi$, as from equation 28, the amplitude of the wave in D_2 approaches zero. Figures showing example waves corresponding to equations 25 and 28 are provided in the online supplement.

Now consider the forced equation, equation 23, which following Rotunno (1983), may be solved using Green's method. We first solve for the function $G(\kappa, z)$, which gives the response to a point forcing at z',

$$G_{zz} + m^2 n(z)^2 G = \delta(z - z') \tag{31}$$

for arbitrary z', where δ is the Dirac delta function, with $\hat{\psi}$ then given by

$$\hat{\psi}(z) = \frac{1}{2\mathcal{A}^2} e^{-\mathcal{L}\kappa} \int_0^\infty G(z, z') e^{-z'} \, dz'. \tag{32}$$

We require G be continuous at z', and by integrating equation 31 over $(z' - \epsilon, z' + \epsilon)$ and taking the limit as $\epsilon \to 0$ we obtain the condition

$$\lim_{\epsilon \to 0} \left(\frac{\partial G}{\partial z}(\kappa, z' + \epsilon) - \frac{\partial G}{\partial z}(\kappa, z' - \epsilon) \right) = 1. \tag{33}$$

When $z' \in D_1$, waves forced above z' partially reflect and refract at H_1, as in expression 25. Waves forced below z' perfectly reflect off the rigid lower boundary, resulting in a vertically non-propagating wave below z'. The matching conditions at z' then allow the constant C in expression 25, and the amplitude of the vertically non-propagating wave below z', to be solved for in terms of z'. Thus, for $z' \in D_1$ we obtain

$$G = \begin{cases} -\frac{1}{mP} \left[\frac{\mathcal{N}+1}{2} e^{im(z' - \mathcal{H}_1)} + \frac{1-\mathcal{N}}{2} e^{-im(z' - \mathcal{H}_1)} \right] \sin(mz) & z \in D_1, z \le z', \quad \text{(34a)} \\ -\frac{1}{mP} \sin(mz') \left[\frac{\mathcal{N}+1}{2} e^{im(z - \mathcal{H}_1)} + \frac{1-\mathcal{N}}{2} e^{-im(z - \mathcal{H}_1)} \right] & z \in D_1, z' < z, \quad \text{(34b)} \\ -\frac{1}{mP} \sin(mz') e^{im\mathcal{N}(z - \mathcal{H}_1)} & z \in D_2, \quad \text{(34c)} \end{cases}$$

where

$$P = \frac{1 + \mathcal{N}}{2} e^{-im\mathcal{H}_1} + \frac{1 - \mathcal{N}}{2} e^{im\mathcal{H}_1}. \tag{35}$$

When $z' \in D_2$, a vertically non-propagating wave is forced below z', with partial ducting within D_1, as in expression 28. Above z' we apply the radiation condition. The matching conditions at z' then allow the constant B in expression 28, and the amplitude of the wave above z', to be solved for in terms of z'. Thus, for $z' \in D_2$ we have

$$G = \begin{cases} -\frac{1}{m\bar{R}} e^{im\mathcal{N}(z'-\mathcal{H}_1)} \sin(mz) & z \in D_1, \quad (36a) \\ -\frac{1}{2im\mathcal{N}\bar{R}} e^{im\mathcal{N}(z'-\mathcal{H}_1)} \left[R e^{im\mathcal{N}(z-\mathcal{H}_1)} - \bar{R} e^{-im\mathcal{N}(z-\mathcal{H}_1)} \right] & z \in D_2, z \leq z', \quad (36b) \\ -\frac{1}{2im\mathcal{N}\bar{R}} \left[R e^{im\mathcal{N}(z'-\mathcal{H}_1)} - \bar{R} e^{-im\mathcal{N}(z'-\mathcal{H}_1)} \right] e^{im\mathcal{N}(z-\mathcal{H}_1)} & z \in D_2, z' < z, \quad (36c) \end{cases}$$

where $R = \cos(m\mathcal{H}_1) + i\mathcal{N}\sin(m\mathcal{H}_1)$ as before. Figures showing waves corresponding to the functions $G(\kappa, z)$ are provided in the online supplement.

Equation 32 can be calculated by decomposing the integral into two terms F_1 and F_2, involving forcing below and above $\mathcal{H}_1$ respectively. Explicitly, we have $\hat{\psi} = F_1 + F_2$, where

$$F_1 = \frac{1}{2\mathcal{A}^2} e^{-\mathcal{L}\kappa} \int_0^{\mathcal{H}_1} G(z, z') e^{-z'} \, dz', \quad (37)$$

$$F_2 = \frac{1}{2\mathcal{A}^2} e^{-\mathcal{L}\kappa} \int_{\mathcal{H}_1}^{\infty} G(z, z') e^{-z'} \, dz'. \quad (38)$$

These integrals can be calculated analytically. For instance, if $z \in D_1$, the term F_1 can be calculated by subdividing the interval $(0, \mathcal{H}_1)$ into the subintervals $(0, z)$ and $(z, \mathcal{H}_1)$, and substituting expressions 34b and 34a for G in each case respectively, whereas F_2 can be calculated by substituting expression 36a for G. Note the expressions for G do not depend on the spatial structure of the heating function Q, and can be used with arbitrary Q, provided it is diurnally oscillating. In section 4 we consider an alternative Q function emulating upper-level convective heating.

The solution for ψ_2 proceeds almost identically to that for ψ_1. As in the solutions of Rotunno (1983) and Qian et al. (2009), ψ is then recovered from $\tilde{\psi} = \hat{\psi}_1 e^{it} + \hat{\psi}_2 e^{-it}$ by calculating the inverse Fourier transform in equation 20 numerically. As in previous studies we use a simple trapezoidal rule. The overall solution procedure may thus be summarised as follows.

1. Non-dimensionalize and combine the governing equations into a single partial differential equation (PDE) for the stream function ψ.

2. Perform a Fourier transform with respect to x, and consider the $e^{\pm it}$ modes separately.

		Figure Numbers				
		2, 3, 4	5, 6, 7	8	13, 14	15, 16
		Heating Function				
		Surface		n/a	Convective	
Dimensional Parameters	N_1 $\left[\mathrm{s}^{-1}\right]$	0.01	0.01	n/a	0.01	0.01
	N_2 $\left[\mathrm{s}^{-1}\right]$	0.03	0.03	n/a	0.025	0.025
	H [km]	1	1	n/a	12	12
	H_1 [km]	2	1.5	n/a	17	15
	H_2 [km]	n/a	2.5	n/a	n/a	19
	L [km]	50	50	n/a	100	100
	D [km]	n/a	n/a	n/a	4	4
	Q_0 $\left[10^{-5}\mathrm{m\,s}^{-3}\right]$	1.2	1.2	n/a	0.6	0.6
	ϕ [deg]	0	0	0	-11.5	-11.5
Non-Dim. Nums.	$\mathcal{N} = \frac{N_2}{N_1}$	3	3	3	2.5	2.5
	$\mathcal{H}_1 = \frac{H_1}{H}$	2	1.5	2	$\frac{17}{12}$	$\frac{15}{12}$
	$\mathcal{H}_2 = \frac{H_2}{H}$	n/a	2.5	$[2,6]$	n/a	$\frac{19}{12}$
	$\mathcal{L} = \frac{\omega L}{N_1 H}$	$\frac{25\pi}{216}$	$\frac{25\pi}{216}$	n/a	$\frac{25\pi}{432}$	$\frac{25\pi}{432}$
	$\mathcal{D} = \frac{D}{H}$	n/a	n/a	n/a	$\frac{1}{3}$	$\frac{1}{3}$
	$\mathcal{A} = \sqrt{1 - \frac{f^2}{\omega^2}}$	1	1	1	≈ 0.92	≈ 0.92

TABLE 1. The parameters used for the various example solutions presented in this study, noting f is the Coriolis parameter and ω the angular frequency of the earth. See text for the definitions of each parameter and non-dimensional number. Non-applicable parameters are marked with n/a. The surface and convective heating functions are given by equations 6 and 55, and depicted in Figs. 1 and 12, respectively.

3. Solve the resulting PDE analytically using Green's method.

4. Recover ψ by performing the inverse Fourier transform numerically using the trapezoid rule.

We now consider an illustrative example solution, presented in dimensional coordinates to aid intuition. We state the governing parameters in dimensional coordinates, with the corresponding non-dimensional numbers provided in Table 1. We set the coastal width parameter $L = 50\,\mathrm{km}$, the heating depth $H = 1\,\mathrm{km}$, Brunt-Väisälä frequencies $N_1 = 0.01\,\mathrm{s}^{-1}$ and $N_2 = 0.03\,\mathrm{s}^{-1}$, giving $\mathcal{N} = 3$, $H_1 = 2\,\mathrm{km}$, and the coastline occurring at the equator so that $f = 0$. Following Du et al. (2019), a

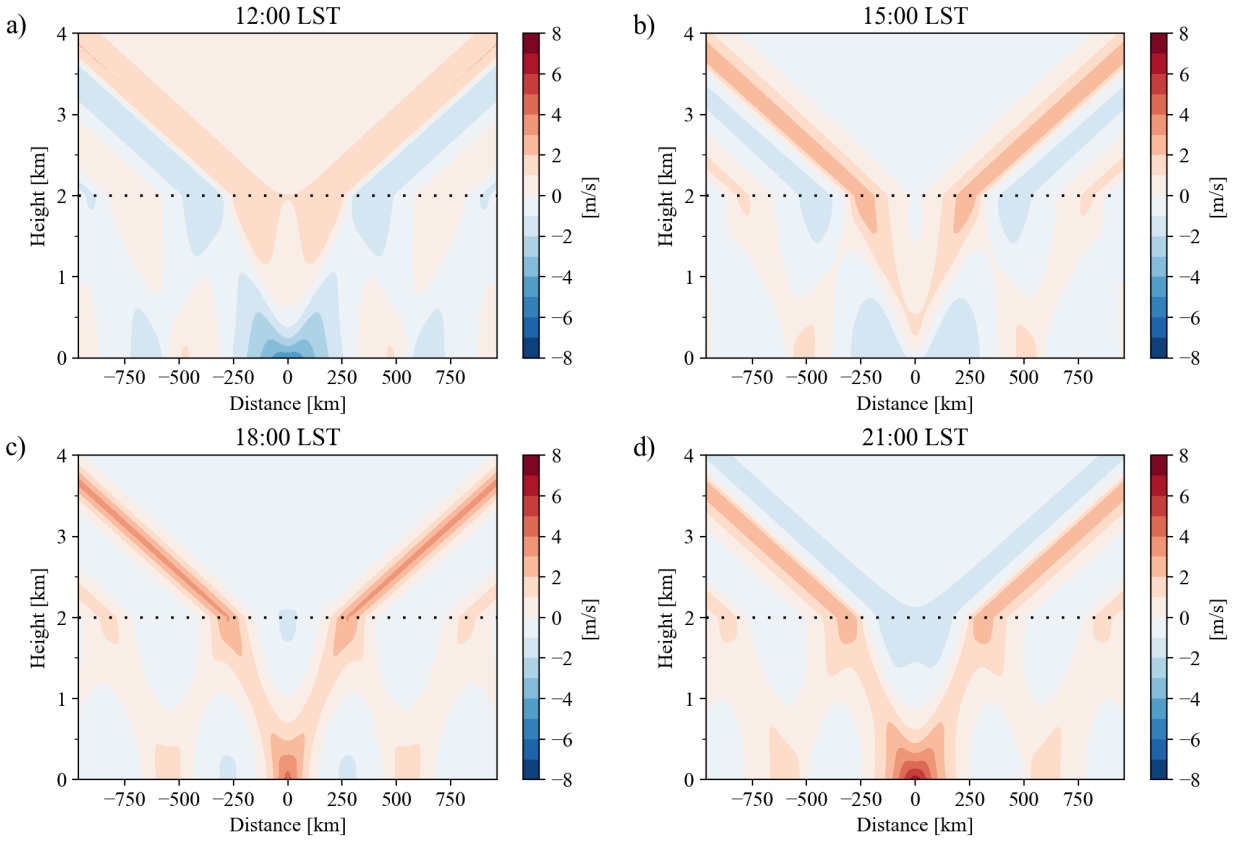

FIG. 2. Coastline perpendicular vertical cross-sections of the piecewise-constant solution for the coastline perpendicular horizontal winds in dimensional coordinates u^* at, a), 12:00 LST, b) 15:00 LST, c) 18:00 LST and d) 21:00 LST, noting that these times correspond to values of 0 h, 3 h, 6 h and 9 h for t^* respectively. The horizontal coordinate x^* gives distance from the coastline. The coastal width is $L = 50\,\text{km}$, the heating depth $H = 1\,\text{km}$, and Brunt-Väisälä frequencies are $N_1 = 0.01\,\text{s}^{-1}$ and $N_2 = 0.03\,\text{s}^{-1}$, giving $\mathcal{N} = 3$. The change in stability occurs at $z^* = H_1 = 2\,\text{km}$, as indicated by the horizontal dotted line. The heating amplitude is $Q_0 = 1.2 \times 10^{-5}\,\text{m}\,\text{s}^{-3}$.

representative heating amplitude of $Q_0 = 1.2 \times 10^{-5}\,\text{m}\,\text{s}^{-3}$ was derived by integrating equation 6 at the surface and far inland between sunrise and sunset, assuming a temperature change of 10 K.

Figure 2 depicts the example solution's coastline perpendicular horizontal velocity u^*. Close to the coastline $x^* = 0$ and near the surface the solution resembles that of Rotunno (1983), with a land breeze evident at 12:00 LST (noon), and persisting until the sea-breeze becomes established at the surface around 15:00 LST, with the largest values of u^* occurring around 21:00 LST. At 00:00 LST (midnight, not shown), Figs. 2 a) to d) repeat, but with colours inverted. As in the solution of Rotunno (1983), wave rays emanate from the origin, and propagate both offshore

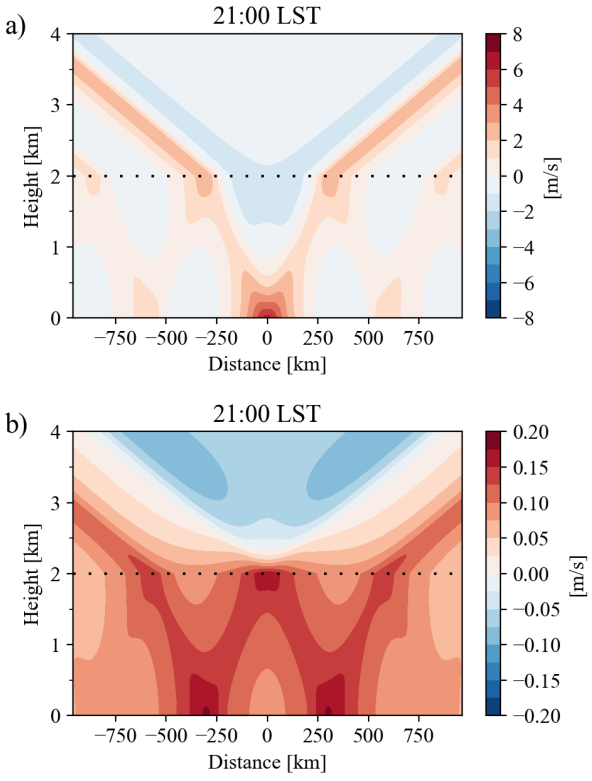

FIG. 3. As in Fig. 2 but for, a), the horizontal velocities u^* resulting from heating F_1 below the stability change at $H_1 = 2\,\text{km}$, and b), heating F_2 above H_1. Note the difference in color-bar scales, with the overall solution depicted in Fig. 2 determined almost entirely by F_1.

and inland. However, unlike in the solution of Rotunno (1983), the rays are partially reflected and partially refracted at $\mathcal{H}_1$. Where the partially reflected ray meets the surface, it is perfectly reflected, producing echoes of the sea-breeze far offshore and far inland from the sea-breeze proper. Further still from the coastline the twice reflected ray again partially reflects and partially refracts at $\mathcal{H}_1$. This continues indefinitely, but with a little more energy escaping from D_1 to D_2 with each refraction, so that for all $z \in D_1$, $u^*(x,z) \to 0$ as $x \to \pm\infty$. This behaviour is similar to that for the low-level inversion, modelled by a discontinuity in potential temperature, considered by Jiang (2012b).

Figures 3 a) and b) decompose the u^* winds at 21:00 LST shown in Fig. 2 d) into those resulting from F_1 and F_2 respectively, i.e. from heating below and above H_1 respectively. Given the structure of Q^*, heating is concentrated in the first 1 km of the atmosphere, and hence the overall solution is almost entirely determined by F_1. The response to the upper level forcing shown in Fig. 3 b)

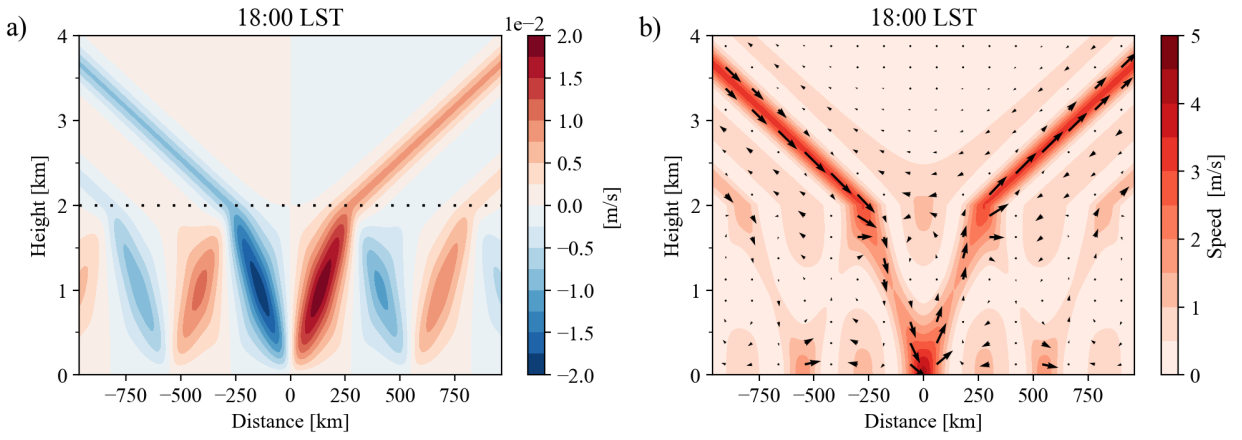

245 FIG. 4. As in Fig. 2 but for, a), the vertical velocity in dimensional coordinates w^*, and b), the velocity field
246 in dimensional coordinates (u^*, w^*), with arrows and shading illustrating the direction and magnitude of the
247 velocity vectors.

242 resembles a St. Andrew's cross, but with the the rays below H_1 reflecting off the lower boundary,
243 and successively reflecting and refracting at H_1 as before. In the supporting online material we
244 consider an example where F_2 is large enough to affect the overall solution.

248 Figures 4 a) and b) illustrate the vertical velocity w^* and the velocity field (u^*, w^*) respectively,
249 at 18:00 LST (sunset). In both cases the reflection and refraction behaviour discussed above is
250 clear. Away from the surface, and away from the change in stability $z^* = H_1$, velocity vectors along
251 the wave rays are essentially parallel with the rays themselves, in accordance with theory. Near
252 the surface, and for values of z just below H_1, the velocity field represents the super-positioning of
253 rays reflecting off the surface, and off the change in stability at $z^* = \mathcal{H}_1$, respectively.

254 The reflection, refraction and ducting coefficients defined above apply to the amplitudes of
255 the stream functions and vertical velocities associated with individual waves. For the horizontal
256 velocities, the refraction coefficient acquires an additional factor of $\mathcal{N}$ in the numerator, and the
257 ducting coefficient in the denominator. Furthermore, while the ducting coefficient depends on
258 $m = \frac{\kappa}{\mathcal{A}}$, the reflection and refraction coefficients do not. The linearity of the inverse Fourier
259 transform therefore implies that, far away from the forcing, the amplitudes of the reflected and
260 refracted rays are also governed by r_1 and r_2, as evident in Fig. 2. Furthermore, the reflection,
261 refraction and ducting behaviours all follow from the Green's function G, which is independent

of the spatial structure of the heating function Q, implying these effects will generalize to other diurnal heating functions.

3. Transition Layer Solution

In this section we consider how the solution presented in section 2 changes when the stability N varies linearly between N_1 and N_2 over a transition-layer $H_1 \leq z^* < H_2$, rather than experiencing a discontinuity. Explicitly, we assume

$$N(z) = \begin{cases} N_1 & 0 \leq z^* \leq H_1, \\ N_1 + (z^* - H_1)M & H_1 < z^* \leq H_2, \\ N_2 & H_2 < z^*, \end{cases} \tag{39}$$

where $M = \frac{N_2 - N_1}{H_2 - H_1}$ is the slope of N in the transition-layer. Equation 23 may then be derived as in the piecewise-constant case, but with the function $n(z)$ now given by

$$n(z) = \begin{cases} 1 & 0 \leq z \leq \mathcal{H}_1, \\ 1 + (z - \mathcal{H}_1)\mathcal{M} & \mathcal{H}_1 < z \leq \mathcal{H}_2, \\ \mathcal{N} & \mathcal{H}_2 < z, \end{cases} \tag{40}$$

where $\mathcal{H}_1 = \frac{H_1}{H}, \mathcal{H}_2 = \frac{H_2}{H}, \mathcal{N} = \frac{N_2}{N_1}$, and $\mathcal{M} = \frac{\mathcal{N}-1}{\mathcal{H}_2 - \mathcal{H}_1}$. We define the vertical subdomains $D_1 = [0, \mathcal{H}_1]$, $D_{\mathrm{TL}} = (\mathcal{H}_1, \mathcal{H}_2]$, $D_2 = (\mathcal{H}_2, \infty)$. Analogously to the piecewise constant N case, we require that $\hat{\psi}$ and $\hat{\psi}_z$ be continuous at both $\mathcal{H}_1$ and $\mathcal{H}_2$.

Before solving equation 23, consider its unforced analogue, equation 24. For $z \in D_1$ and $z \in D_2$, equation 24 reduces to the same pair of wave equations as the piecewise-constant N case, with analogous general solutions. However, for $z \in D_{\mathrm{TL}}$, equation 24 becomes

$$\hat{\psi}_{zz} + m^2(1 + (z - \mathcal{H}_1)\mathcal{M})^2\hat{\psi} = 0. \tag{41}$$

This is a form of Weber's equation, the general solution of which is the linear combination of two parabolic cylinder functions (e.g. Whittaker and Watson 1996) $D_a(z)$ and $D_b(z)$, where

$$D_a(z) = D_{-\frac{1}{2}}((1+i)Z(z)), \tag{42}$$

$$D_b(z) = D_{-\frac{1}{2}}((1-i)Z(z)), \tag{43}$$

with $D_{-\frac{1}{2}}$ the parabolic cylinder function of argument $-\frac{1}{2}$, noting we have defined the convenience function $Z : [\mathcal{H}_1, \mathcal{H}_2) \to \left[\frac{\sqrt{m}}{\sqrt{|\mathcal{M}|}}, \frac{\sqrt{m}\mathcal{N}}{\sqrt{|\mathcal{M}|}}\right)$ by

$$Z(z) = \sqrt{\frac{m}{|\mathcal{M}|}}(1 + \mathcal{M}(z - \mathcal{H}_1)), \tag{44}$$

so that Z is both positive and real. To see that $D_a(z)$ and $D_b(z)$ satisfy equation 41, note that for an arbitrary variable $\zeta \in \mathbb{C}$, the function $D_\nu(\zeta)$ satisfies the differential equation (e.g. Wünsche 2003)

$$\left(\frac{d^2}{d\zeta^2} - \frac{\zeta^2}{4} + \nu + \frac{1}{2}\right) D_\nu(\zeta) = 0. \tag{45}$$

In the case of $\nu = -\frac{1}{2}$, equation 45 reduces to

$$\left(\frac{d^2}{d\zeta^2} - \frac{\zeta^2}{4}\right) D_{-\frac{1}{2}}(\zeta) = 0. \tag{46}$$

Substituting the variable $\zeta = (\pm 1 \pm i)Z(z)$, it follows

$$\frac{d^2}{d\zeta^2} D_{-\frac{1}{2}}((\pm 1 \pm i)Z(z)) = -m^2(1 + \mathcal{M}(z - \mathcal{H}_1)) D_{-\frac{1}{2}}((\pm 1 \pm i)Z(z)). \tag{47}$$

Thus $D_a(z)$ and $D_b(z)$ satisfy equation 41. Physically, the functions $D_a(z)$ and $D_b(z)$, describe how upward and downward propagating waves are modulated as they pass through the transition-layer: further details are provided in appendix A1 and the online supplement.

Equation 23 is again solved using Green's method. The Green's function G can be obtained by considering the $z' \in D_1$, $z' \in D_{\mathrm{TL}}$, and $z' \in D_2$ cases separately, as in the piecewise constant N case. The resulting expressions are analogous to those for the piecewise-constant solution, but more complex to state, and so are relegated to appendix A2. Equation 32 can then be decomposed

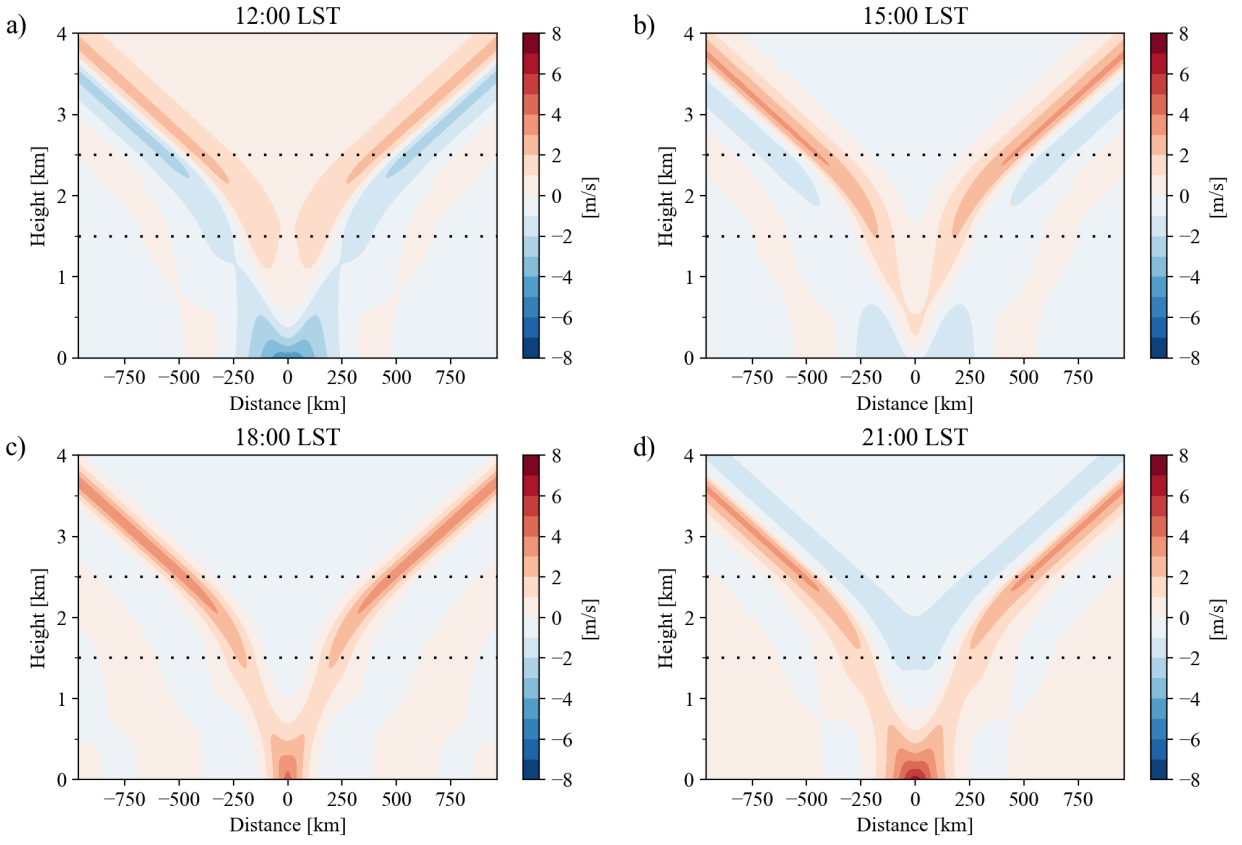

FIG. 5. As in Fig. 2, but for the transition-layer solution for the coastline-perpendicular horizontal winds u^*. The transition-layer begins at $z^* = H_1 = 1.5\,\mathrm{km}$ and ends at $z^* = H_2 = 2.5\,\mathrm{km}$, as depicted by the horizontal dotted lines, with $N_1 = 0.01\,\mathrm{s}^{-1}$ and $N_2 = 0.03\,\mathrm{s}^{-1}$, so that $\mathcal{N} = 3$, as before.

$\hat{\psi} = F_1 + F_{\mathrm{TL}} + F_2$, analogously to before, where F_1, F_{TL} and F_2 now result from the heating below, within and above the transition-layer respectively, noting F_{TL} must be calculated numerically. We can then solve for ψ, u and w by calculating the inverse Fourier transforms numerically as before.

Figure 5 provides an illustrative example solution for the coastline perpendicular horizontal velocity u^*, with the same choices of parameters as in the piecewise-constant example solution depicted in Fig. 2, but with a transition-layer starting at $z^* = H_1 = 1.5\,\mathrm{km}$ and ending at $z^* = H_2 = 2.5\,\mathrm{km}$ (see Table 1). The behaviour of the horizontal winds in Fig. 5 near the surface, close to the coastline, is essentially identical to the piecewise constant solution. However, away from the surface, and away from the coastline, the behaviour of the rays is notably different. The rays now refract smoothly, with the slope of the rays changing gradually over the transition-layer. Moreover, ray reflection is substantially reduced, being only just visible in the weakest red and blue

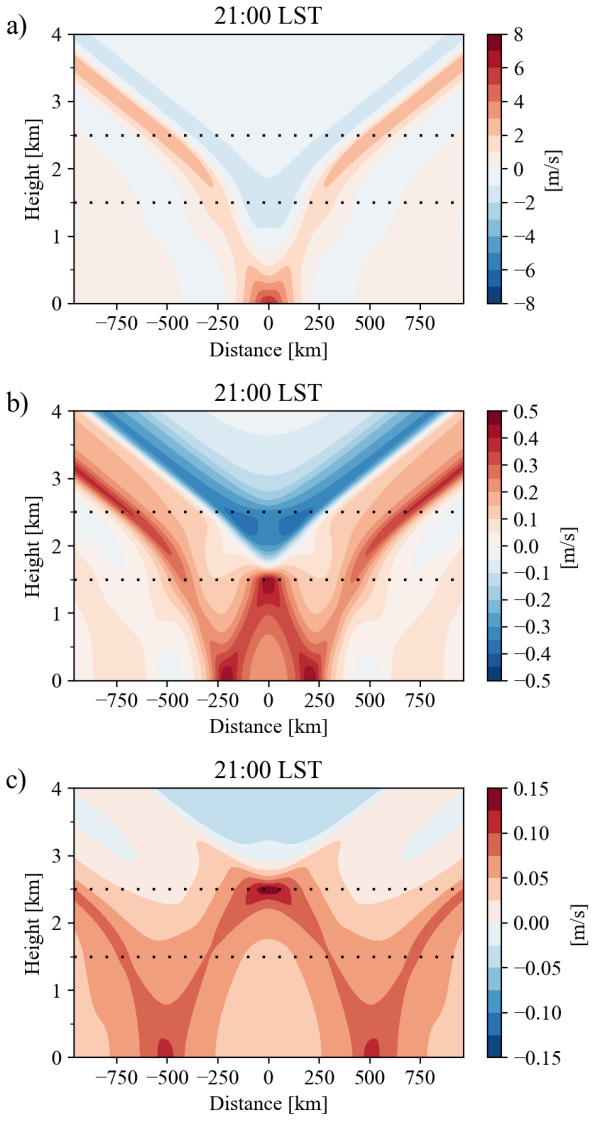

FIG. 6. As in Fig. 5 but for, a), the horizontal velocities u^* resulting from heating F_1 below $H_1 = 1.5\,\mathrm{km}$, b), heating F_{TL} within the transition-layer between $H_1 = 1.5\,\mathrm{km}$ and $H_2 = 2.5\,\mathrm{km}$, and c), heating F_2 above H_2. Note the difference in color-bar scales, with the overall solution depicted in Fig. 5 determined almost entirely by F_1.

shaded regions. For transition-layer solutions corresponding to larger values of $\mathcal{N}$ (not shown), ray reflection becomes more evident, but the amplitude of the reflected ray is always less than in the corresponding piecewise-constant solution.

Figures 6 a), b) and c) decompose the u^* winds at 21:00 LST shown in Fig. 5 d) into those resulting from F_1, F_{TL} and F_2 respectively, i.e. from heating below, within and above the transition-layer. As in the piecewise-constant solution, the overall response is almost entirely determined by F_1, but

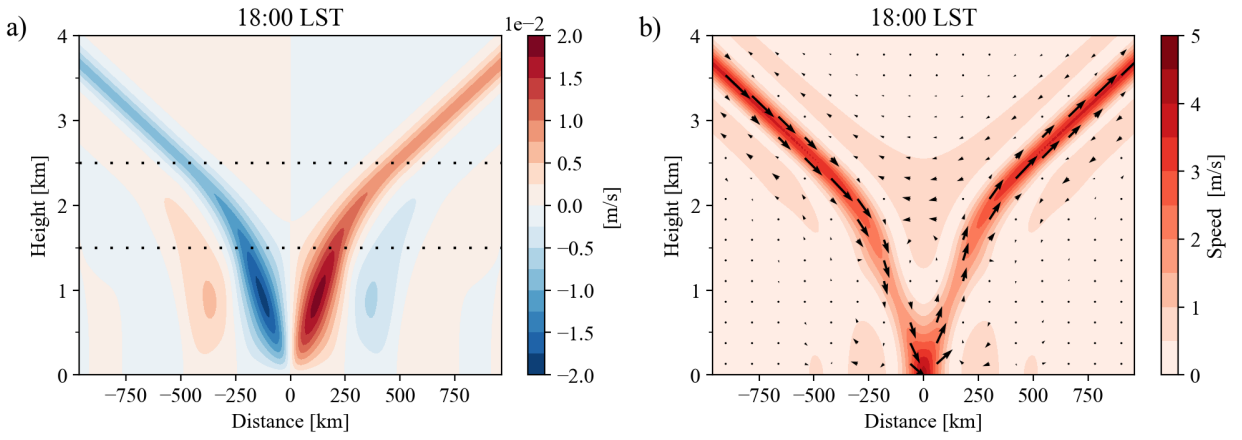

FIG. 7. As in Fig. 4, but for the transition-layer solutions for, a), w^*, and b), the velocity field (u^*, w^*).

ray reflection is substantially reduced, as noted above. The responses to F_{TL} and F_2 resemble the St. Andrew's cross, but with smooth ray refraction through the transition-layer.

Figures 7 a) and b) illustrate the vertical velocity w^*, and the velocity field (u^*, w^*) respectively, at 18:00 LST (sunset). The smooth refraction behaviour is again evident, with less overall ray reflection than the piecewise-constant solution. Furthermore, the maximum speeds along the rays in D_2 are $\approx 0.5\,\mathrm{m\,s^{-1}}$ faster in the transition-layer solution than in the piecewise constant solution depicted in Fig. 4 b), representing an increase of $\approx 15\%$.

To determine the generality of the observed differences between the piecewise constant and transition-layer solutions, consider again the reflection, refraction and ducting coefficients, r_1, r_2 and r_3, this time obtained by taking ratios of wave amplitudes in D_1 and D_2 from the expressions given in appendix A2. Figure 8 provides example values for these coefficients for $\mathcal{H}_1 = 2$, $\mathcal{N} = 3$, and a range of values for $\mathcal{H}_2 \geq \mathcal{H}_1$, and the non-dimensional vertical wavenumber m. As discussed in appendix A2, these coefficients converge to their values in the piecewise-constant solution as $\mathcal{H}_2 \to \mathcal{H}_1$, but as $\mathcal{H}_2 - \mathcal{H}_1 \to \infty$ we also have the limits,

$$r_1 \to 0, \quad r_2 \to \frac{1}{\sqrt{\mathcal{N}}}, \quad r_3 \to \sqrt{\mathcal{N}}. \tag{48}$$

We will refer to the $\mathcal{H}_2 \to \mathcal{H}_1$ and $\mathcal{H}_2 - \mathcal{H}_1 \to \infty$ limits as the short and long limits respectively. The long limits are plotted as dashed grey lines in Figs. 8 a) to d), and it is evident that for larger wavenumbers, the transition-layer depth $\mathcal{H}_2 - \mathcal{H}_1$ does not need to be particularly large before r_1,

331 r_2 and r_3 are approximately equal to their long limits. In appendix A2 we derive conditions for
332 approximate convergence to the long limit: for $\mathcal{N} > 1$,

$$\frac{\lambda}{\mathcal{H}_2 - \mathcal{H}_1} \ll \frac{16\pi}{3(\mathcal{N}-1)}, \tag{49}$$

333 and for $\mathcal{N} < 1$,

$$\frac{\lambda}{\mathcal{H}_2 - \mathcal{H}_1} \ll \frac{16\pi\mathcal{N}^2}{3(1-\mathcal{N})}, \tag{50}$$

334 where $\lambda = \frac{2\pi}{m}$ is the non-dimensional vertical wavelength in D_1. For example, for the $m = 4$
335 coefficients plotted in brown in Figs. 8 a), b) and d), inequality 49 reduces to $\mathcal{H}_2 - \mathcal{H}_1 \gg \frac{3}{16} = 0.19$,
336 and approximate convergence therefore occurs when $\mathcal{H}_2 - \mathcal{H}_1$ is about an order of magnitude larger
337 than 0.19, i.e. $\mathcal{H}_2 > \mathcal{H}_1 + 2 = 4$. Figures 8 a), b) and d) indicate this is indeed the case, noting that
338 r_1 converges more slowly than r_2 and r_3.

339 Similarly, approximate convergence to the short limit occurs when

$$\frac{\lambda}{\mathcal{H}_2 - \mathcal{H}_1} \gg \frac{\pi\mathcal{N}^2}{\mathcal{N}-1} \tag{51}$$

340 for $\mathcal{N} > 1$, and

$$\frac{\lambda}{\mathcal{H}_2 - \mathcal{H}_1} \gg \frac{\pi}{1-\mathcal{N}} \tag{52}$$

341 for $\mathcal{N} < 1$. Again considering the $m = 4$ coefficients in Fig. 8, inequality 51 reduces to $\mathcal{H}_2 - \mathcal{H}_1 \ll \frac{1}{9}$,
342 so that $\mathcal{H}_2 < 2.01$. Thus for $m = 4$, the reflection, refraction and ducting coefficients depart from
343 their short limit values substantially, for even a small transition-layer.

349 The short limit expression for the ducting coefficient r_3 depends on both m and $\mathcal{H}_1$, and for
350 particular choices of these values, the short limit for r_3 may be either larger or smaller than the
351 long limit. However, for the reflection and refraction coefficients r_1 and r_2, the long and short
352 limit expressions depend only on $\mathcal{N}$, not on m, $\mathcal{H}_1$ or $\mathcal{H}_2$. Furthermore, the short limit for the
353 reflection coefficient $r_1 = \left|\frac{1-\mathcal{N}}{1+\mathcal{N}}\right|$ is strictly greater than the long limit $r_1 = 0$ for $\mathcal{N} > 0$, $\mathcal{N} \neq 1$.
354 Analogously, the short limit for the refraction coefficient $r_2 = \frac{2}{\mathcal{N}+1}$ is strictly less than the long limit
355 $r_2 = \frac{1}{\sqrt{\mathcal{N}}}$ for $\mathcal{N} > 0$, $\mathcal{N} \neq 1$. While r_1 and r_2 oscillate as the depth of the transition-layer increases,
356 suggesting resonance between the vertical wavelength and the depth of the transition-layer, r_1 and

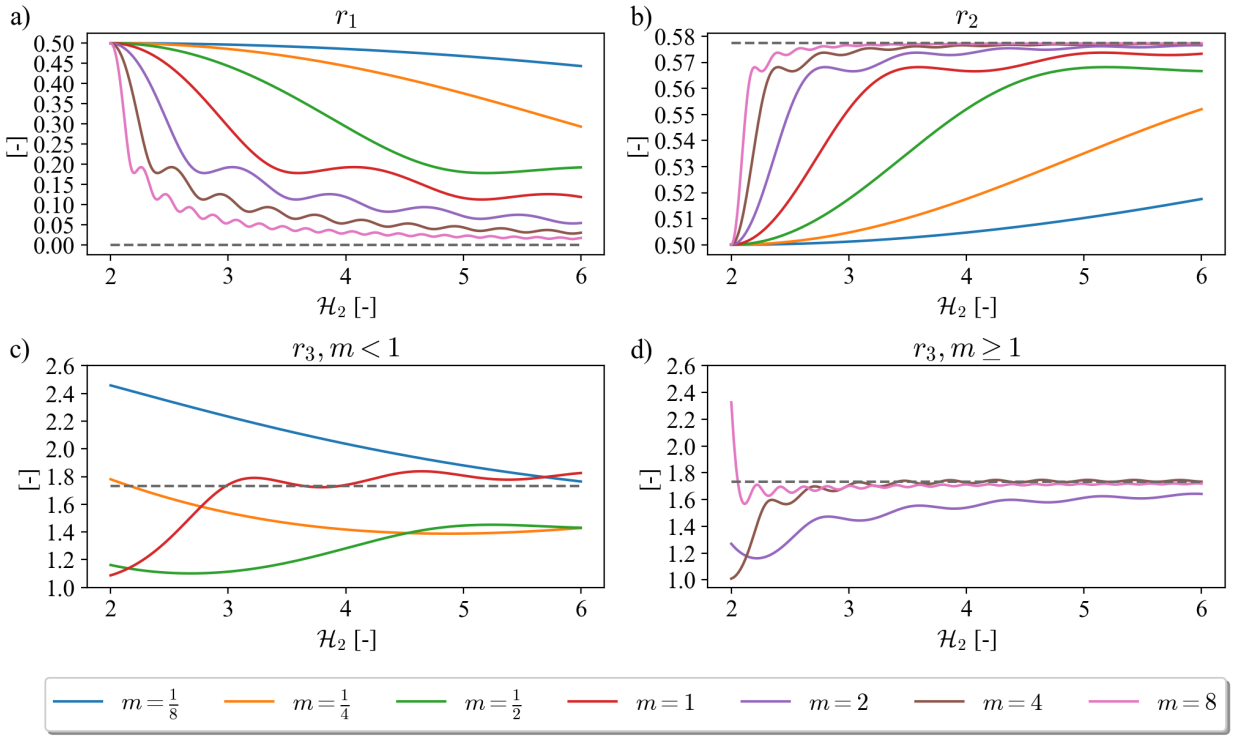

FIG. 8. Plots illustrating how, a), the reflection coefficient r_1, b), the refraction coefficient r_2, and c) and d), the ducting coefficient r_3, change as the transition-layer deepens, for various values of the non-dimensional vertical wavenumber m, noting $m = m^* H$, where m^* is the wavenumber in dimensional coordinates, and H is the heating depth. The transition-layer begins at $z = \mathcal{H}_1 = 2$, with $\mathcal{N} = 3$. Dashed grey lines show the large $\mathcal{H}_2 - \mathcal{H}_1$ limit values 0, $\frac{1}{\sqrt{\mathcal{N}}}$ and $\sqrt{\mathcal{N}}$ for the coefficients r_1, r_2 and r_3 respectively.

r_2 are bounded by their long and short limit values. Thus, waves reflect less, and refract more, in the presence of a transition-layer, than when stability changes discontinuously.

To provide physical intuition for this result, consider again the problem of an unforced atmosphere with no lower boundary, a step-change in stability at $\mathcal{H}_1$, and a radiation condition imposed above $\mathcal{H}_1$. Suppose first $\mathcal{N} > 1$, and that instead of both upward and downward propagating waves in D_1, there is just a single wave in D_1. At a height sufficiently far below $\mathcal{H}_1$, vertical parcel displacements associated with this wave are contained entirely in D_1, but as z approaches $\mathcal{H}_1$, vertical parcel displacements impinge on D_2. Because stability increases in D_2, the total upward displacement experienced by the parcel will be smaller if it enters D_2 than if stays entirely within D_1. Specifically, a parcel oscillating about $z = \mathcal{H}_1$ is displaced a greater distance downward from

$\mathcal{H}_1$ than upward. However, because the upward and downward phases of its oscillation must each occur over the same length of time, i.e. half the diurnal period, the vertical velocity w must be discontinuous at H_1. But this violates conservation of mass: the continuity equation $u_x + w_z = 0$ cannot be satisfied as w_z would then be infinite at $\mathcal{H}_1$, whereas u_x would remain finite. Thus, to conserve mass there must be a second wave in D_1, i.e. the reflected wave, which offsets the negative vertical displacements associated with the incident wave.

Consider now the analogous transition-layer case, where stability increases by the same amount overall, but the change occurs linearly between $\mathcal{H}_1$ and $\mathcal{H}_2$, again assuming $\mathcal{N} > 1$. Suppose there is just a single wave in D_1. As z approaches $\mathcal{H}_1$, parcels displaced upward from z must move through the transition-layer D_{TL} before potentially reaching D_2, with the stability throughout D_{TL} lower than that in D_2. For a parcel originally at $\mathcal{H}_1$, the upward displacement is again smaller in magnitude than the downward displacement, but larger in magnitude than the upward-displacement when stability is piecewise constant. Thus, to conserve mass, the amplitude of the reflected wave must be smaller in the transition-layer case than in the piecewise-constant case, as the difference between the magnitudes of the upward and downward displacements is smaller in the latter case than the former. This argument also shows why the amplitude of the reflected wave must approach zero as $\mathcal{H}_2 - \mathcal{H}_1 \to \infty$. Analogous arguments apply when $\mathcal{N} < 1$. Linear displacement fields for the piecewise-constant and transition-layer example solutions are provided in the online supplement, which assist in visualising the preceding arguments.

While the limits in expression 48 can be derived in a direct way mathematically, they can also be inferred indirectly, albeit informally. Consider individual sinusoidal wave perturbations (u, v, w), i.e. perturbations whose spatial structure in x is given by $e^{i\kappa x}$ for some wavenumber κ. Suppose these perturbations occur against a horizontal background wind $(\overline{u}, 0, 0)$. Under the Bousinesq approximation on an f-plane, the temporal rate of change of the mean background-state horizontal velocity $\overline{u}$ is given by the convergence of mean specific wave momentum flux (e.g. Sutherland 2010),

$$\frac{\partial \overline{u}}{\partial t} = -\frac{\partial \langle uw \rangle}{\partial z}, \tag{53}$$

where angle brackets denote the average over a horizontal wavelength in the x direction. Because $\overline{u} = \frac{\partial \overline{u}}{\partial t} = 0$ by construction in our study, the mean specific momentum flux $\langle uw \rangle$ must be constant in z. Suppose the amplitude of the vertical velocity of the incident wave is A. From the parcel

argument given above, in the long limit the amplitude of the reflected wave is zero, so

$$\langle uw \rangle = \begin{cases} \frac{-A^2}{2} & z \in D_1, \quad (54a) \\ \frac{-\mathcal{N}A^2 r_2^2}{2} & z \in D_2. \quad (54b) \end{cases}$$

Thus, in the long limit, the refraction coefficient r_2 must be $\frac{1}{\sqrt{\mathcal{N}}}$ to ensure the specific momentum flux is constant. Analogous considerations apply for the ducting coefficient r_3.

For a transition-layer of finite, non-zero thickness, r_1 and r_2 depend on m, and the reflection and refraction coefficients of the rays will lie somewhere between the long and short limit values for the component waves comprising the rays. As the thickness of the transition-layer increases, inequalities 49 and 50 imply a greater proportion of the ray's wavenumber spectrum behaves according to the long limit, rather than the short limit. Thus, the reflection and refraction coefficients for the rays will also approach the long limits 0 and $\frac{1}{\sqrt{\mathcal{N}}}$ as $\mathcal{H}_2 - \mathcal{H}_1 \to \infty$. Similarly, inequalities 51 and 52 imply the reflection and refraction coefficients of the rays converge to the short limit expressions for r_1 and r_2 as $\mathcal{H}_2 \to \mathcal{H}_1$. Analogous arguments apply to the ducting coefficient for the rays, with the amplitude of the ducted ray approaching $\sqrt{\mathcal{N}}$ as $\mathcal{H}_2 - \mathcal{H}_1 \to \infty$. Analogously to the piecewise-constant solution, the reflection, refraction and ducting behaviours in the transition-layer solution follow from the Green's function G given in appendix A2, implying these effects will again generalize to other diurnal heating functions Q.

4. Years of the Maritime Continent Soundings

The original motive for formulating the transition-layer problem was to interpret a set of radiosonde observations obtained from the second Australian leg of the Years of the Maritime Continent (YMC) field campaign during November and December 2019 (Yoneyama and Zhang 2020; Protat and McRobert 2020b; Protat et al. 2022). During this campaign, the RV Investigator, Australia's scientific research vessel, sailed through the waters near Darwin, the capital of Australia's Northern Territory, as depicted in Fig. 9. Between the 20/11/19 and 02/12/19, the Investigator travelled from the waters north-west of Darwin, past Croker Island, and back again, launching 8 radiosondes per day as it did so.

Figure 10 illustrates the vertical profile of the Brunt-Väisälä frequency N obtained from the soundings taken between 20/11/2019 - 02/12/19. The light grey line depicts the profile of N at

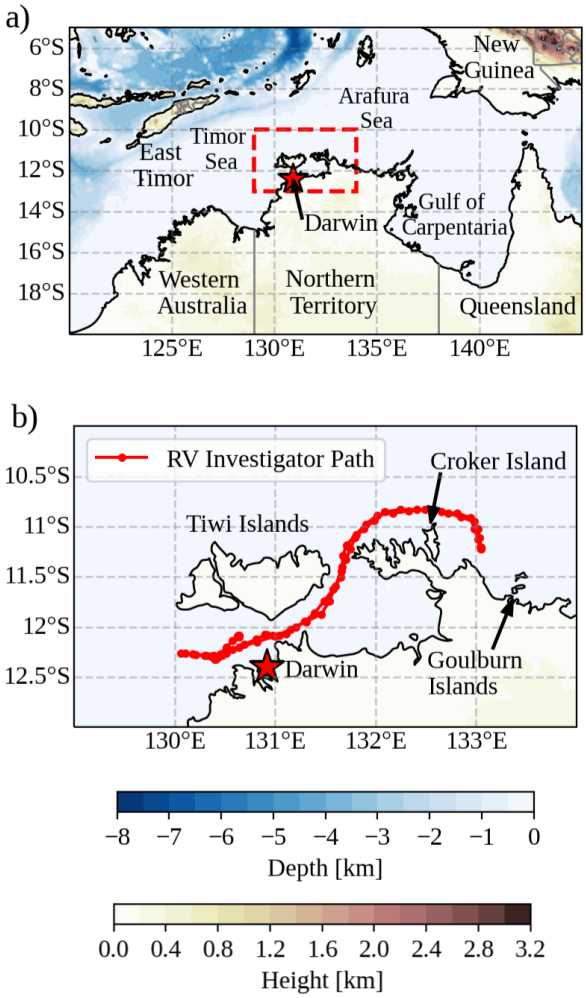

FIG. 9. Maps depicting, a), Australia's Northern Territory, its capital Darwin, and surrounding landmarks, and b), the region within the red-dashed line box in a), showing the location of the RV Investigator between the 20th of November and the 2nd of December 2019.

00:00 LST on 20/11/2019, and the dark grey line the average over this day. The thicker black line provides the average over the entire 20/11/2019 - 02/12/19 time period, with a 200 m running mean applied to reduce the small scale noise. Note the average profile of N is $\approx 0.01\,\mathrm{s}^{-1}$ below $\approx 15\,\mathrm{km}$ and $\approx 0.025\,\mathrm{s}^{-1}$ above $\approx 19\,\mathrm{km}$, transitioning roughly linearly between these two values between these two heights. This structure is not an artifact of the averaging: it is also present, albeit in a noisier form, in the grey lines. Furthermore, an N transition-layer is consistent with previous work demonstrating that under various tropopause definitions utilizing diverse variables,

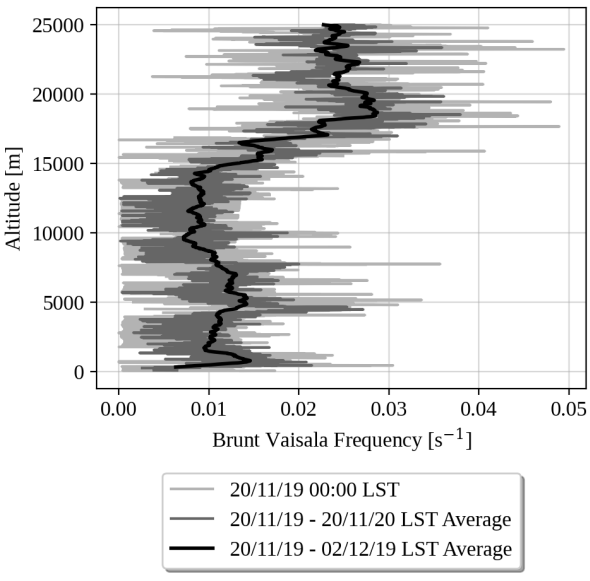

FIG. 10. The vertical profile of the Brunt-Väisälä frequency N from the soundings obtained during the portion of the RV Investigator voyage depicted in Fig. 9 b). The light grey line depicts the Brunt-Väisälä frequency at 00:00 LST on 20/11/2019, the dark grey line depicts the average over 20/11/2019, while the thicker black line depicts the average over the entire 20/11/2019 - 02/12/19 period, with a 200 m running-mean applied to this average to further smooth small scale noise.

the tropopause resembles a transition-layer, rather than a discontinuity (Pan et al. 2004; Schmidt et al. 2006; Fueglistaler et al. 2009; Feng et al. 2012).

Figure 11 a) provides a Hövmöller diagram of the meridional winds from the soundings between 00:00 local solar time (LST) on 20/11/2019 and 00:00 LST on 02/12/2019, with winds linearly interpolated in time onto a regular hourly time-step. White regions indicate missing values, where the radiosonde's balloon burst before ascending above 25 km. Note there is significant vertical shear in the meridional winds, particularly between $\approx 8-17$ km. Recall that we assumed background winds were zero in the theory presented in sections 2 and 3, as sheared background winds significantly complicate the analytic approach (Du et al. 2019): our theory should therefore be applied cautiously to this YMC dataset. Nevertheless, note the weak stratospheric meridional background winds above ≈ 17 km in Fig. 11 a), with clear downward propagating diurnal perturbations.

Figure 11 b) provides the corresponding Hövmöller diagram of the wind perturbations against a 24-hour centred running mean background wind, with missing values interpolated linearly when

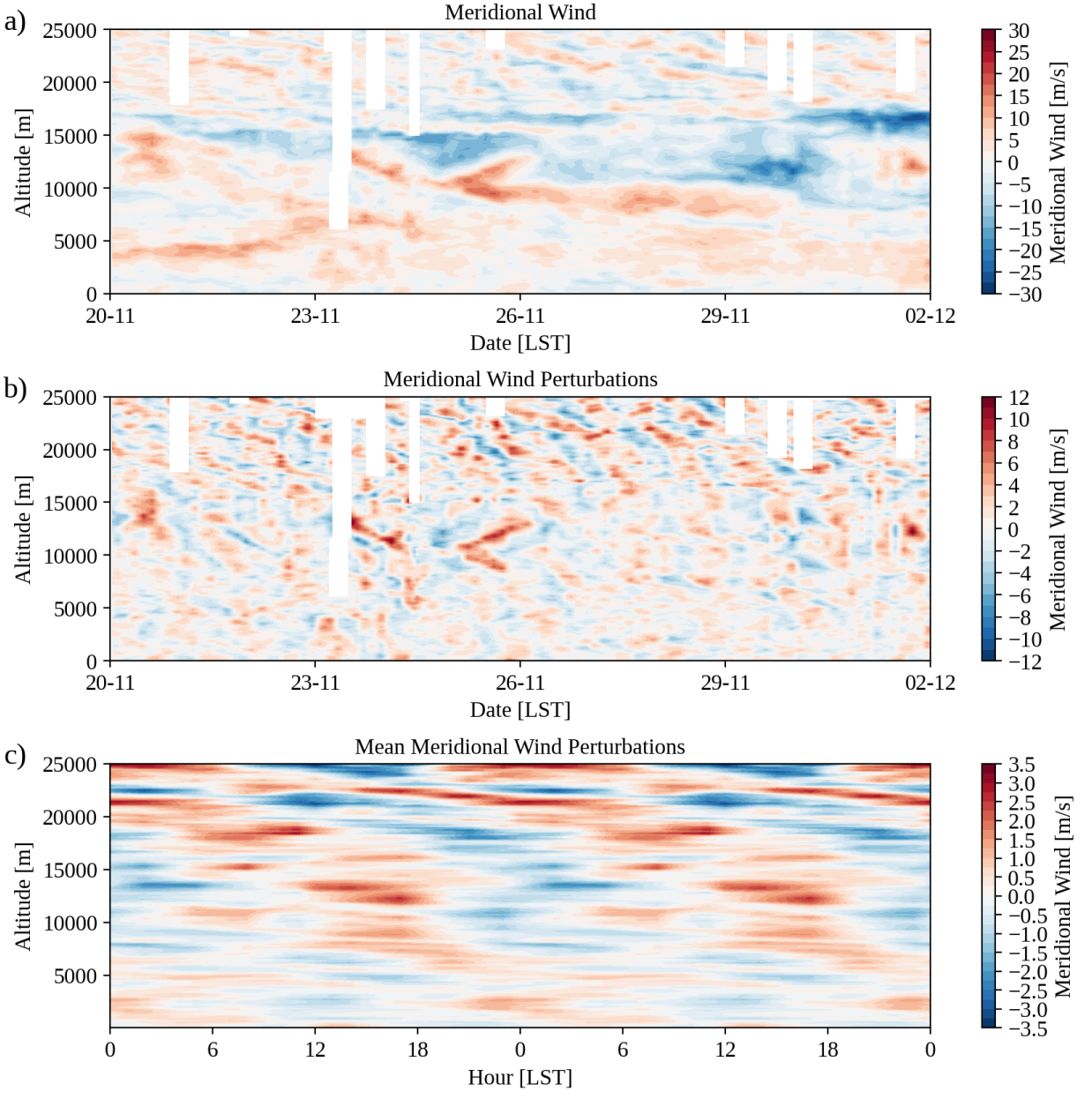

435 FIG. 11. Hövmöller diagrams of, a), the meridional winds, b), the meridional wind perturbations against a
436 24 hour centred running mean background wind, and c), the average perturbations at each time of day, from the
437 soundings taken on board the RV Investigator between 20/11/2019 - 02/12/19. The location of the RV Investigator
438 during this period is depicted in Fig. 9 b).

450 calculating the background wind, but not the perturbations. Diurnal perturbations are now evident
451 throughout both the stratosphere and troposphere. Sometimes the tropospheric perturbations also

propagate downward, but at a faster vertical phase speed than those in the stratosphere, while at other times they are essentially stationary. Figure 11 c) provides a Hövmöller diagram of the composite diurnal cycle, obtained by averaging the perturbations depicted in Fig. 11 b) at each hour of the day: the cycle is repeated once for clarity. A downward propagating signal is again evident in the stratosphere, with the signal more stationary below 15 km, and showing a degree of discontinuity at ≈ 4 km. Note that in Figs. 17 b) and c), the magnitude of the winds above 17 km are of comparable or greater magnitude than those below 17 km.

Suppose we interpret the perturbations in Figs. 11 b) and c) as representing gravity wave rays forced at the diurnal frequency. Such waves would likely have multiple sources, including the immediate Australian coastline, remote coastlines, and nearby and remote diurnal cycles of convection. The basic solution of Rotunno (1983), and Figs. 2 and 5, suggest that wave rays forced at the surface along a coastline wouldn't reach the stratosphere until thousands of kilometres away from that coastline. Over such distances, the rays would likely disperse through the effect of background winds, friction, and violations of the f-plane assumption.

Suppose then that the waves are forced nearby, but at upper-levels. Indeed, Hankinson et al. (2014) applied ray tracing methods to stratospheric gravity waves observed in radiosonde observations over Darwin, concluding the waves originated from convection over Indonesia, the Phillipines and New Guinea. In particular, Hankinson et al. (2014) attributed the lower-stratospheric waves with vertical wavelengths of 2-4 km, similar magnitudes to those of the stratospheric signals in Fig. 11, to New Guinea convection. Furthermore, in a high-resolution simulation, Vincent and Lane (2016, Fig. 15) documented wave rays forced along the northern New Guinea coastline, with additional rays forced at upper-levels around 12 km altitude, roughly in phase with those forced near the surface. These upper level rays were likely forced by the convective and stratiform heating associated with the convective line that occurs daily over the New Guinea mountain range during Austral Summer.

To emulate the upper-level heating associated with a convective line, we redefine

$$Q^* = Q_0 \exp\left(-\frac{x^{*2}}{L^2} - \frac{(z^* - H)^2}{D^2}\right)\cos(\omega t^*), \tag{55}$$

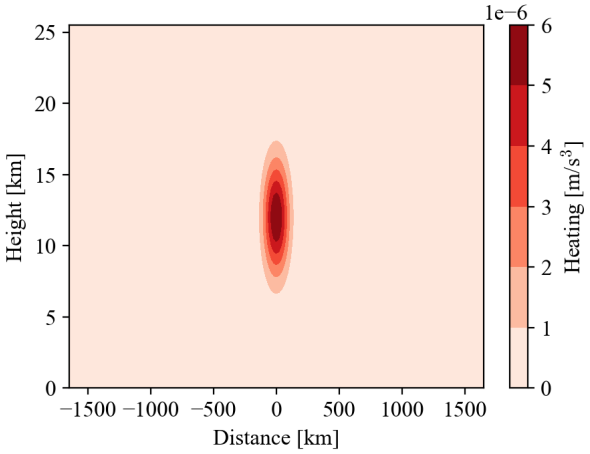

Fig. 12. The heating function given by equation 55 at noon LST, i.e. $t^* = 0$, with $L = 100\,\mathrm{km}$, $H = 12\,\mathrm{km}$, $D = 4\,\mathrm{km}$ and $Q_0 = 6\times10^{-6}\,\mathrm{m\,s^{-3}}$.

where L and D give the horizontal and vertical scales of a two-dimensional Gaussian heating function centred at $x^* = 0$, and $z^* = H$, similar to the function considered by Robinson et al. (2008). Figure 12 provides an example of the new heating function, with $L = 100\,\mathrm{km}$, $H = 12\,\mathrm{km}$, $D = 4\,\mathrm{km}$ and $Q_0 = 6\times10^{-6}\,\mathrm{m\,s^{-3}}$.

With the heating function given by equation 55, equation 32 becomes

$$\hat{\psi}(z) = \frac{1}{2\mathcal{A}^2} i\sqrt{\pi}k\mathcal{L}e^{-\frac{k^2\mathcal{L}^2}{4}} \int_0^\infty G(z,z')e^{-\frac{(z'-1)^2}{\mathcal{D}^2}}\,dz', \tag{56}$$

where $\mathcal{L} = \frac{\omega L}{N_1 H}$ and $\mathcal{D} = \frac{D}{H}$, with the Green's function G given by the same expressions as in section 2 and appendix A2. Analytic solutions to equation 56 can then be given in terms of the Gaussian error function, with the exception of the transition-layer solution when $z' \in D_{\mathrm{TL}}$, which must be solved numerically as before.

Figure 13 presents an example piecewise constant solution using the revised heating function, with $H_1 = 17\,\mathrm{km}$, $L = 100\,\mathrm{km}$, $D = 4\,\mathrm{km}$ and $H = 12\,\mathrm{km}$ (see Table 1). It is somewhat unclear how Q_0 should be chosen: as a first guess we take $Q_0 = 6\times10^{-6}\,\mathrm{m\,s^{-3}}$, half that of the surface forcing considered in sections 2 and 3, with this choice motivated by the potential temperature tendencies and perturbations in the simulation and observational results of Vincent and Lane (2016, 2018). From Fig. 10 we take $N_1 = 0.01\,\mathrm{s^{-1}}$, $N_2 = 0.025\,\mathrm{s^{-1}}$, so that $\mathcal{N} = 2.5$. We choose an f-plane based on a constant latitude of 11.5° south.

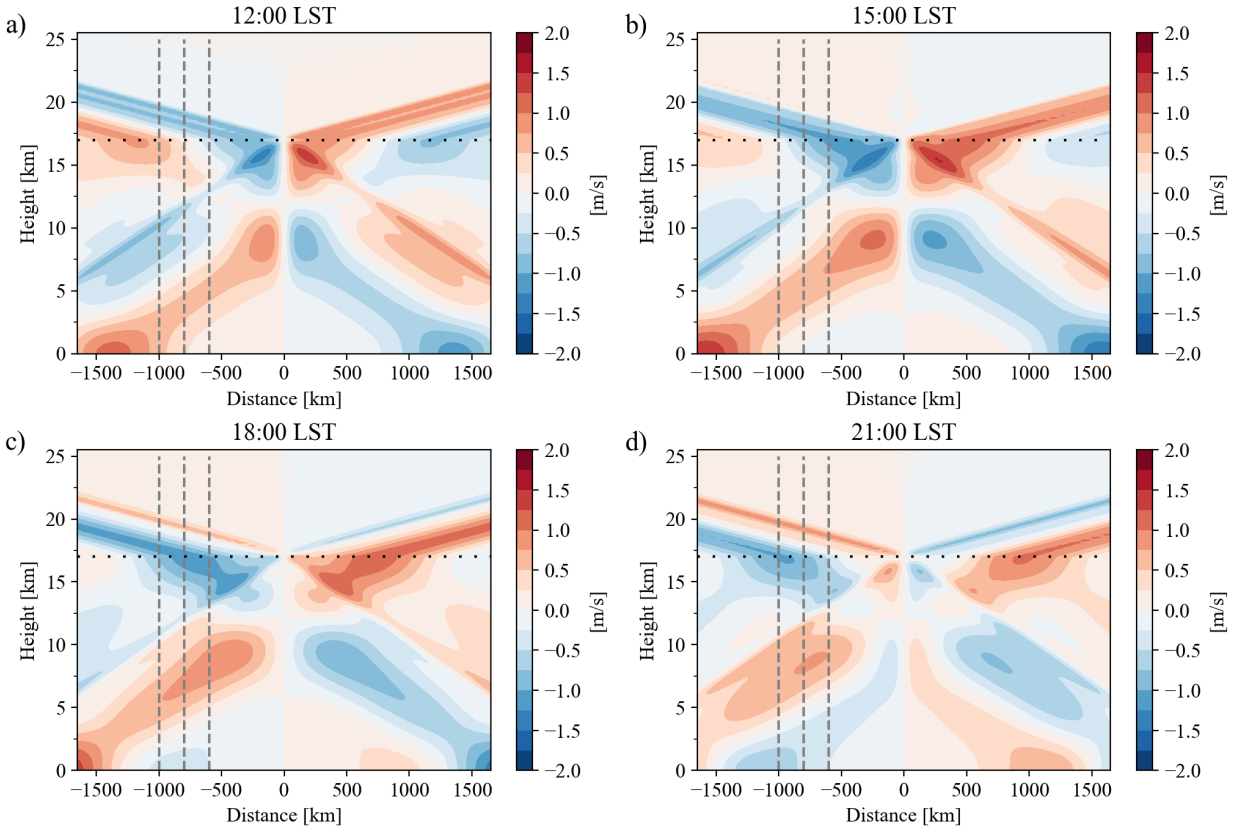

Fig. 13. The piecewise constant solution for the convective-line-perpendicular horizontal winds u^*, using the heating function given by equation 55, with $H_1 = 17\,\mathrm{km}$, $L = 100\,\mathrm{km}$, $D = 4\,\mathrm{km}$, $H = 12\,\mathrm{km}$, and $Q_0 = 6\times10^{-6}\,\mathrm{m\,s^{-3}}$. The Brunt-Väisälä frequencies are $N_1 = 0.01\,\mathrm{s^{-1}}$, $N_2 = 0.025\,\mathrm{s^{-1}}$, so that $\mathcal{N} = 2.5$, and the f-plane is chosen based on a constant latitude of 11.5° south. Depicted are the winds at, a), 12:00 LST, b) 15:00 LST, c) 18:00 LST and d) 21:00 LST. The vertical grey dashed lines at $x^* = -600\,\mathrm{km}$, $-800\,\mathrm{km}$ and $-1000\,\mathrm{km}$ show the vertical transects considered in Fig. 17.

A St. Andrew's cross pattern is evident in Fig. 13, with reflection and refraction of the upper rays at H_1. The reflected rays, which are narrow, superpose on the lower-rays forced at 12 km. Vertical phase speeds associated with the upper-rays are negative as before, but positive for the lower rays, as required by the radiation condition. Also, the horizontal winds are now out of phase either side of $x^* = 0$, physically consistent with the convergence/divergence associated with a localised heating function: mathematically, this occurs because Q_x is now a dipole rather than a monopole.

Figure 14 decomposes the 15:00 LST horizontal winds depicted in Fig. 13 b) into those arising from F_1 and F_2 respectively, i.e. forcing below and above the stability change at $H_1 = 17\,\mathrm{km}$. As in

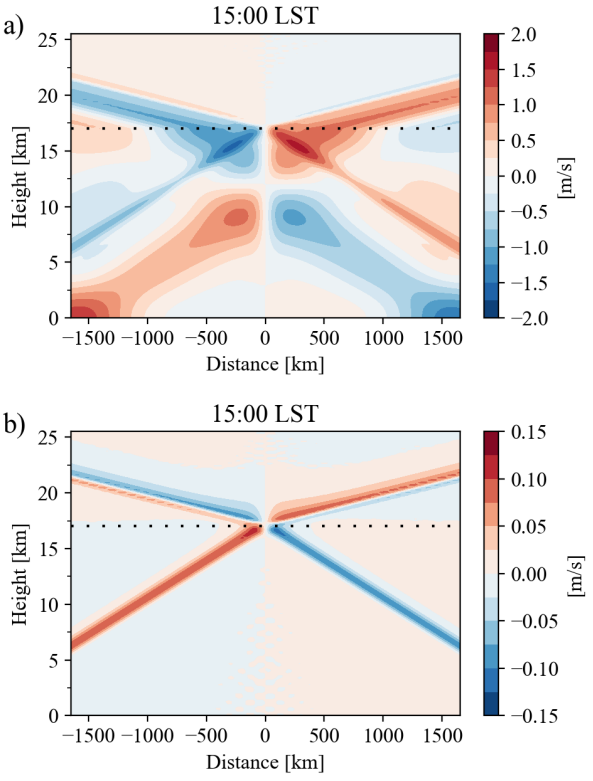

FIG. 14. As in Fig. 13 but for, a), the horizontal velocities u^* at 15:00 LST resulting from heating F_1 below the stability change at $H_1 = 17\,\text{km}$, as depicted by the horizontal dotted line, and b), heating F_2 above H_1. Note the difference in color-bar scales, with the overall solution depicted in Fig. 13 determined mostly by F_1.

section 2, the overall response is mostly determined by F_1, recalling that the heating is concentrated at $H = 12\,\text{km}$.

Figure 15 provides the corresponding transition-layer solution, with $H_1 = 15\,\text{km}$ and $H_2 = 19\,\text{km}$ (see Table 1). As before, the rays reflect less than in the piecewise-constant solution, with more energy escaping into the stratosphere. Figure 16 decomposes the 15:00 LST u^* winds depicted in Fig. 15 b) into those arising from F_1, F_{TL}, and F_2 respectively, i.e. heating below, within and above the transition-layer between $H_1 = 15\,\text{km}$ and $H_2 = 19\,\text{km}$. Although the reflected ray in Fig. 16 is seemingly of larger magnitude than the reflected ray in the piecewise constant solution in 14 a), the domains D_1 encompass different heights in each case, and when considered with the response to the heating within the transition-layer F_{TL}, the apparent increased reflection is almost completely offset, so that the net reflection is less than in the piecewise-constant case.

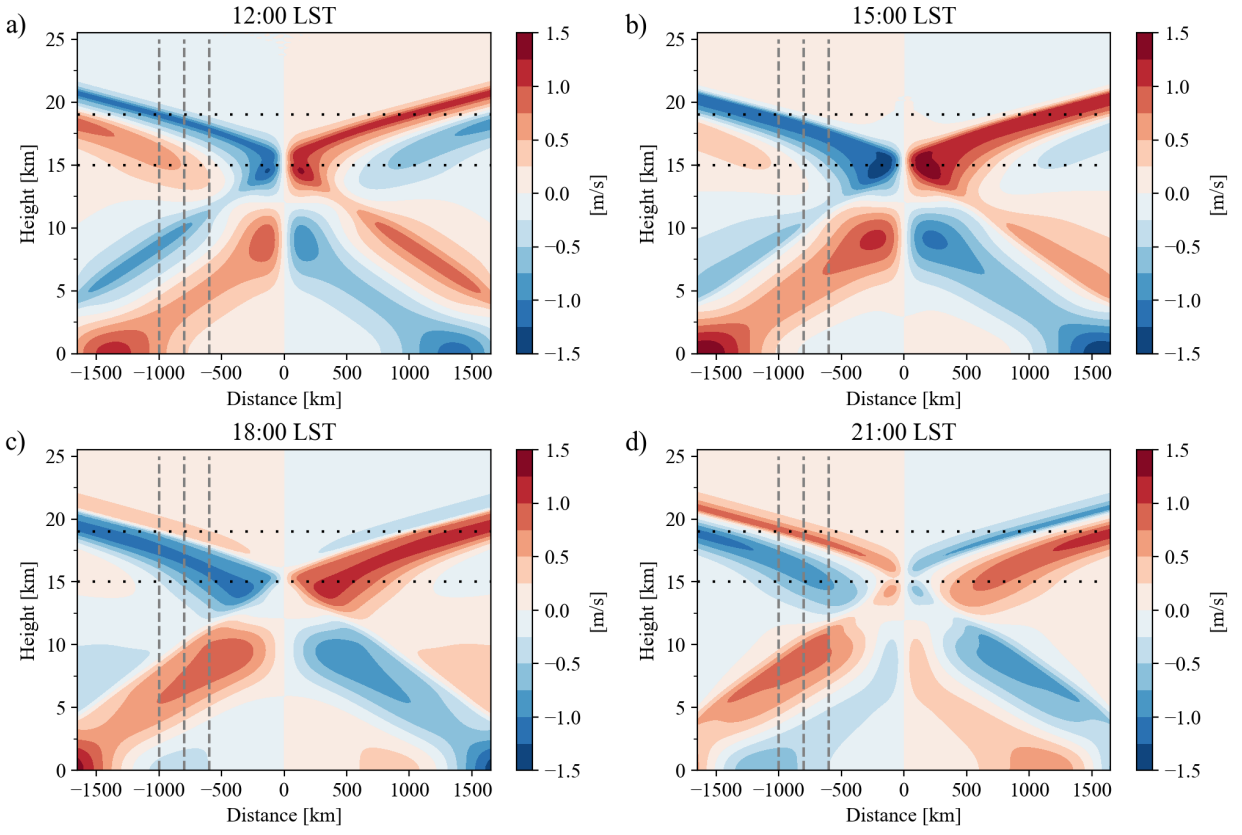

FIG. 15. As in Fig. 13, but for the transition-layer solution, with $H_1 = 15\,\text{km}$ and $H_2 = 19\,\text{km}$, as depicted by the horizontal dotted lines.

To qualitatively compare the solutions above with the YMC soundings, suppose we interpret $x^* = 0$ as the position of a daily recurring convective line oriented roughly perpendicular to the displacement vector from the convective line to the RV Investigator. Following the discussion above, we might take $x^* = 0$ as the position of the New Guinea mountain range, with the y^* direction then extending along the range. We could then view the RV Investigator as being located some distance in the negative x^* direction, and the meridional winds depicted in Fig. 11 as loosely corresponding to the convective-line-perpendicular winds u^* in Figs. 13 and 15.

Figure 17 a) provides a Hövmöller diagram of the u^* winds along the vertical transects at $x = -600\,\text{km}$, $-800\,\text{km}$ and $-1000\,\text{km}$, depicted by the dashed grey lines in Figs. 13 and 15. There are qualitative similarities, but also notable differences, between the Hövmöller diagrams in Figs. 11 and 17. Each of the diagrams in Fig. 17 features negative phase speeds above 12 km, consistent with Fig. 11. In the transition-layer solution, the horizontal wind speeds above 17 km are

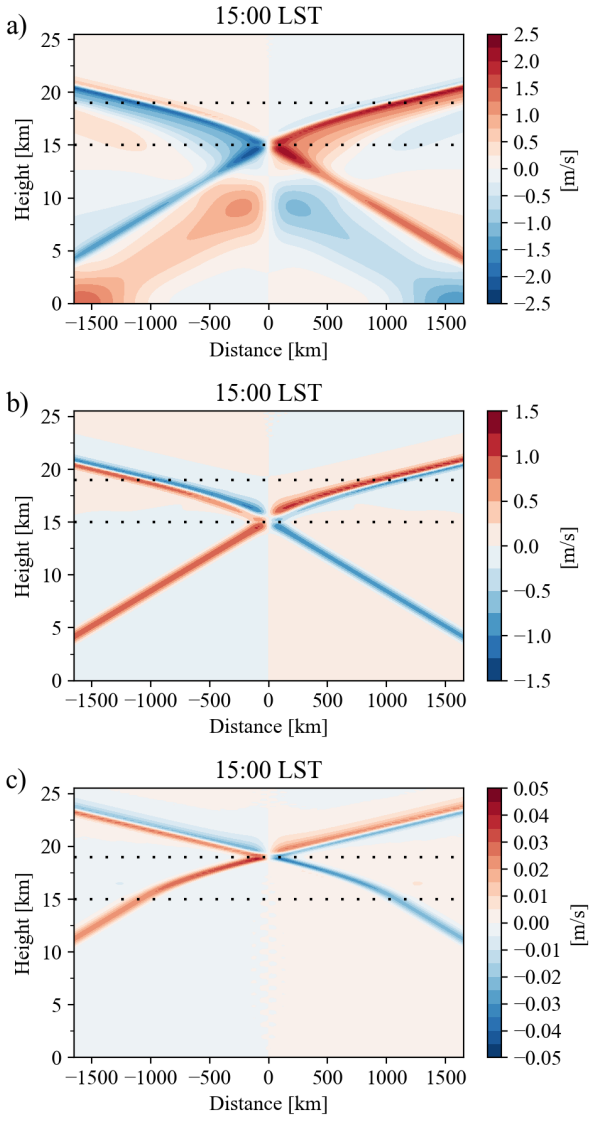

FIG. 16. As in Fig. 15 but for the horizontal velocities u^* at 15:00 LST resulting from, a), heating F_1 below $H_1 = 15\,\text{km}$, b), heating F_{TL} within the transition-layer between $H_1 = 15\,\text{km}$ and $H_2 = 19\,\text{km}$, and c), heating F_2 above H_2. Note the difference in color-bar scales, with the overall solution depicted in Fig. 15 determined mostly by F_1 and F_{TL}.

at least $0.25\,\text{m}\,\text{s}^{-1}$, or $\approx 20\%$, larger than in the piecewise-constant solution. Moreover, the winds directly above and below 17 km are of comparable magnitude, and the overall signal smoother, compared with the piecewise-constant solution, which is more erratic due to increased reflection and discontinuous refraction. This suggests the transition-layer solution more realistically simulates the transfer of energy through the tropopause than the piecewise-constant solution.

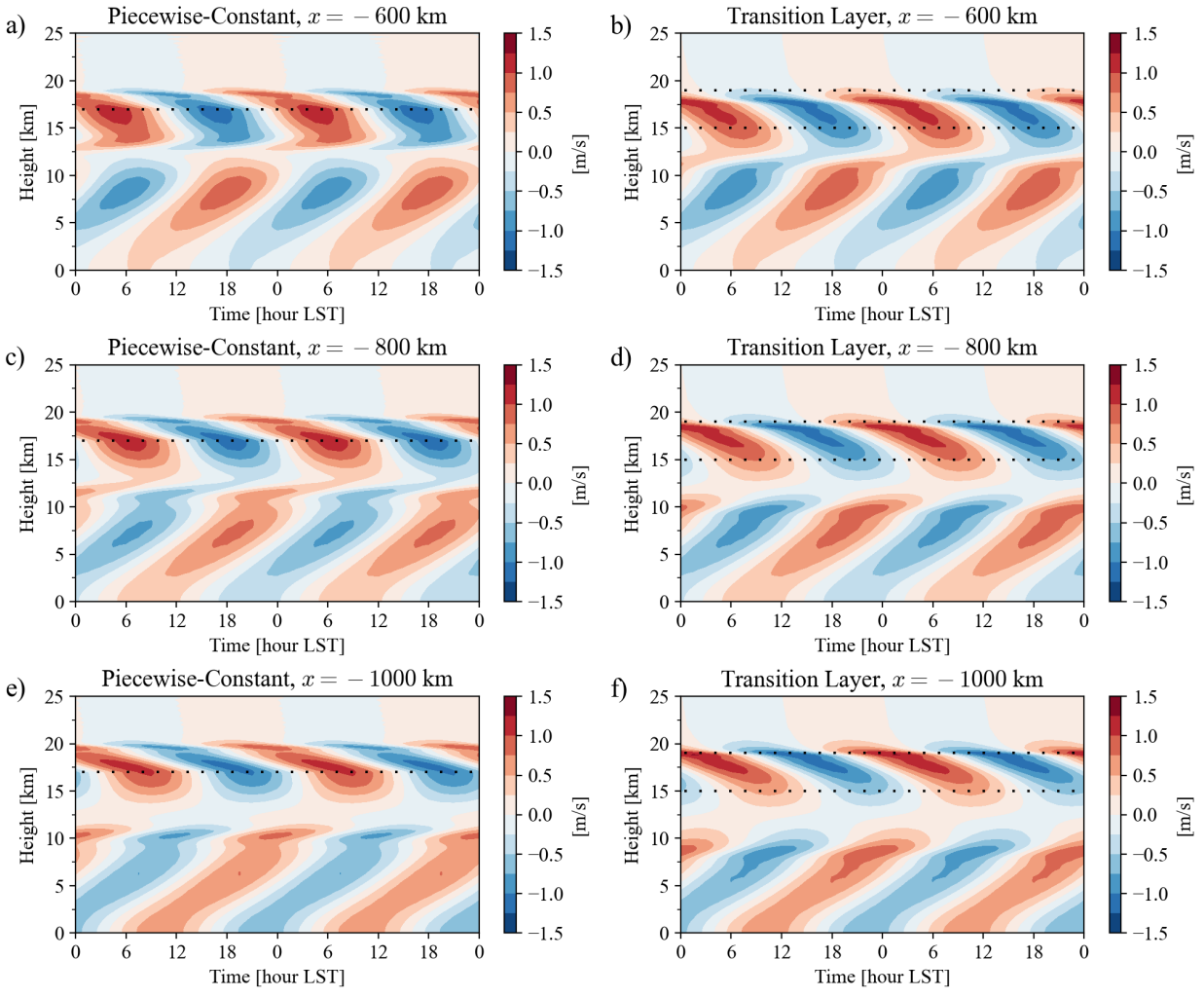

FIG. 17. Hövmöller diagrams of the convective-line-perpendicular horizontal winds u^* from, a), c), e), the piecewise-constant solution, and b), d) e), the transition-layer solutions depicted in Figs. 13 and 15 along the grey dashed vertical transects at, a), b), $x^* = -600$ km, and c), d), $x^* = -800$ km and e), f), $x^* = -1000$ km. The heights of the stability changes H_1 and H_2 are depicted by the horizontal dotted lines.

Timings and magnitudes of the upper level signals are comparable to those in Fig. 11, although the upper level response ends below 20 km in Fig. 17, but extends to at least 25 km in Fig. 11. One explanation for this difference is the lack of background winds in the theory, with background winds in the convective-line-perpendicular direction acting to partially disperse the rays, resulting in more oscillations in the vertical (Qian et al. 2009).

A major difference between Figs. 11 and 17 is in the response below 12 km. In Fig. 17 the perturbations below 12 km exhibit positive vertical phase speeds as discussed above, whereas in Fig. 11 phase speeds are negative, or the signal is stationary. One explanation for this difference is that, in reality, additional surface or low-level convective diurnal heating is present, generating rays with negative phase speeds which superpose with the downward pointing rays with positive phase speeds generated by the upper-level forcing. This super-positioning could result in a signal that is stationary, or downward propagating. The apparent continuity of the upper and lower perturbations in Fig. 11 b) and c) would then be essentially coincidental. These ideas could be critically tested using ray-tracing methods applied to more complex numerical model data (e.g. Hecht et al. 2004; Alexander et al. 2004; Vincent et al. 2004; Hankinson et al. 2014).

To generalise the above ideas, note that the line-parallel winds v^* can be recovered from the line-perpendicular winds u^* using polarisation relations inferred from equation 11, which show that v^* is in quadrature with u^*, with the amplitude of v^* equal to that of u^* scaled by $\frac{f}{\omega}$. The horizontal winds in other directions then comprise weighted sums of u^* and v^*, and hence the essential structure of the solutions depicted in Figs. 13 and 15 will not change if other wind directions are considered. Analogous points apply to rotations of the convective line in the x^*, y^* plane, excluding the degenerate cases of rotations by $\pm 90°$.

5. Discussion and Conclusion

In this study we extended the tropical linear sea-breeze theory of Rotunno (1983) to situations involving non-constant Brunt-Väisälä frequency N. We first presented an illustrative example of a low-level stability change, emblematic of that between the boundary layer and troposphere. Because solutions are formulated using the Green's function G, generalizing to other heating functions Q is straightforward. We therefore also considered an alternative heating function representing diurnally recurrent convective or stratiform heating aloft, and considered how forced waves behave as they passed through the tropopause.

In both cases wave reflection, refraction and ducting behaviour depends not only on the height and magnitude of the stability change, but on the thickness of the transition-layer, at least in the idealised circumstances of the theory. This behaviour follows from the structure of the Green's function G, implying broad generality of this result. It may therefore be instructive to consider

how the solutions presented here behave across diverse climatic conditions, and to compare this behaviour with more realistic numerical simulations, or observations. For example, increases in tropopause height are anticipated under warming (e.g. Hu and Vallis 2019), and this will affect the tropopause reflection, refraction and ducting behaviour in the theory presented here. Furthermore, the thickness of the tropopause transition-layer varies with latitude and season, and there is an observed thickening trend over the last four decades (Schmidt et al. 2006; Feng et al. 2012), with idealised models indicating the structure of the tropopause transition-layer is sensitive to tropospheric warming, stratospheric cooling, and the vertical ozone profile (Lin et al. 2017; Dacie et al. 2019). The solutions presented in this study therefore suggest tropopause wave reflection, refraction and ducting will vary significantly across season and latitude, and potentially also with climate. These hypotheses could be investigated with more realistic modelling experiments.

The solutions also provide test cases for assessing the numerical methods used in more complex models. In particular, if the vertical discretization of a finite-difference based time-stepping numerical method is too coarse over a stability change, we might expect simulated wave rays to reflect and refract as in the piecewise constant solution, rather than the appropriate transition-layer solution, with finite difference based schemes therefore exaggerating the total energy reflected. In the online supplement we provide a preliminary investigation of these ideas.

Simplifying assumptions were made to derive the linear equations considered in this study, as in the related studies described in section 1. Most significant is perhaps linearity itself, which eliminates density current dynamics, an important aspect of the land-sea breeze at low levels near the coast (Qian et al. 2012). Non-linear and non-hydrostatic effects may also be significant in certain contexts (e.g. Pandya et al. 1993, 2000). Furthermore, viscosity may increasingly attenuate wave rays with horizontal distance from their source (Yan and Anthes 1987; Dalu and Pielke 1989), so that if the stability change occurs a large vertical distance from the forcing, reflection and refraction become a moot point.

Another potential limitation is the Bousinesq approximation, which is usually thought to be valid only over vertical scales much less than the density scale height H_ρ, where $H_\rho \approx 8\,\mathrm{km}$ in the troposphere. However, Du et al. (2019) compared a similar set of analytic solutions, involving a non-constant background wind $\overline{u}(z)$ but constant N, to two-dimensional Weather Research and Forecasting model (WRF) simulations, and found a remarkable agreement between the two

throughout the lowest 10 km of the atmosphere. This agreement, in conjunction with the scale analysis of Ogura and Phillips (1962), suggest that in the atmosphere it is actually the potential temperature scale height $H_\theta \approx 30\,\mathrm{km}$ that determines the validity of the Boussinesq approximation. We therefore expect our core results about reflection, refraction and ducting will be unaffected by the Boussinesq approximation, provided the depth of the transition-layer is small compared to H_θ: this could be tested using a similar set of WRF experiments as Du et al. (2019).

The most physically important process missing from the theory presented here is probably background winds, as these not only alter the basic structure of the wave rays (Qian et al. 2009), but changes in background winds with height also induce attenuation, reflection and refraction (Du et al. 2019; Lane 2021) of their own. A straightforward extension of our piecewise-constant solution would be to ignore the Coriolis term, but include constant background winds above and below the stability change, with a discontinuity permitted at the stability change. Analogously, the transition-layer solution could be extended by ignoring Coriolis, but allowing the background winds to shear linearly between the constant values above and below the transition-layer. Equation 41 would then become a form of Whittaker's equation, with Whittaker function solutions, which may permit a similar analysis to that of the present paper.

To summarise, in this study we began by extending the linear sea-breeze theory developed by Rotunno (1983) to include vertical changes in the Brunt-Väisälä frequency N. In section 2 we presented the solution in the case where $N = N_1$ below some height H_1, and $N = N_2$ above H_1, where N_1 and N_2 are constant. The behaviour of this solution is determined by the non-dimensional parameters $\mathcal{A}$, $\mathcal{L}$, $\mathcal{N} = \frac{N_2}{N_1}$ and $\mathcal{H}_1 = \frac{H_1}{H}$. In section 3 we presented the solution for the case where $N = N_1$ below some height H_1, $N = N_2$ above some other height $H_2 > H_1$, with N transitioning linearly between these two values for z^* between H_1 and H_2. The behaviour of this solution is determined by the non-dimensional parameter $\mathcal{H}_2 = \frac{H_2}{H}$, in addition to those for the piecewise constant solution.

In the piecewise constant solution, gravity wave rays emanate from the origin, as in the base solution of Rotunno (1983). These rays are generated by heating below H_1. The individual waves comprising the rays reflect and refract, with the amplitudes of the reflected and refracted waves governed by the coefficients $r_1 = \left|\frac{1-\mathcal{N}}{1+\mathcal{N}}\right|$ and $r_2 = \frac{2}{\mathcal{N}+1}$ respectively. These expressions are the Boussinesq versions of the coefficients derived by Lindzen and Tung (1976). Because these

coefficients are independent of the non-dimensional vertical wavenumber m, the amplitudes of the reflected and refracted rays are also governed by r_1 and r_2.

When stability decreases with height, or H_1 is comparable or smaller than the vertical scale of the heating H, waves forced by heating above H_1 also play a significant role. Below the forcing, the rigid lower boundary implies vertically non-propagating waves are present above and below H_1, with the ratio of their amplitudes given by the ducting coefficient $r_3 = \frac{\mathcal{N}}{\sqrt{\cos^2(m\mathcal{H}_1)+\mathcal{N}^2\sin^2(m\mathcal{H}_1)}}$, or equivalently $r_3 = \frac{\mathcal{N}}{\sqrt{\cos^2(m^*H_1)+\mathcal{N}^2\sin^2(m^*H_1)}}$, where $m^* = \frac{m}{H}$ is the vertical wavenumber in dimensional coordinates. Because r_3 depends on m, the ducting behaviour of the ray depends on the specifics of its wavenumber spectrum.

Overall, the reflection, refraction and ducting behaviour in the transition-layer solution is significantly different from the piecewise-constant solution. The coefficients r_1, r_2 and r_3 now depend on m, but for each m the amplitudes of the reflected wave is lower, and the amplitude of the refracted wave greater, than in the corresponding piecewise constant solution. The reflection, refraction and ducting coefficients approach their piecewise-constant expressions when $H_2 \to H_1$. Furthermore, the reflection, refraction and ducting coefficients approach the limits 0, $\frac{1}{\sqrt{\mathcal{N}}}$ and $\sqrt{\mathcal{N}}$ as $H_2 - H_1 \to \infty$. Because these long limits do not depend on m, as $H_2 - H_1 \to \infty$ the limiting amplitudes of the reflected, refracted and ducted rays are also governed by these coefficients. Away from the forcing, the amplitude of the reflected ray is therefore always lower, and refracted ray higher, in the presence of a transition-layer, than a discontinuity in stability. The change in stability $\mathcal{N}$ does not need to be particularly extreme, nor the thickness of the transition-layer large, before the behaviour of the rays moves away from the piecewise-constant limit, and substantially toward the large limit.

The core reflection, refraction and ducting behaviours described above all follow from the structure of the Green's function G, not the spatial structure of the heating function Q, and it is therefore straightforward to consider other functions Q. In section 4 we considered an alternative heating function which emulates the upper-level convective or stratiform heating associated with a convective line. In this case H is the height at which heating is concentrated, and the solution depends on an additional non-dimensional parameter $\mathcal{D} = \frac{D}{H}$, which describes the vertical depth of the heating. We compared this modified theory to observations taken during the Australian leg of the YMC field campaign, finding the observations showed better qualitative agreement

with the transition-layer solution than the piecewise-constant solution. For realistic values of $\mathcal{N}$, and a realistic thickness of the tropopause transition-layer, there is notably less reflection, and more refraction, in the transition-layer solution than the piecewise-constant solution. As noted by Lindzen and Tung (1976), when modelled as a step-change in stability, the tropopause is "a rather poor reflector": when modelled by a transition-layer, it becomes an outright bad reflector.

Acknowledgments. Funding for this study was provided for Ewan Short by the Australian Research Council's Centre of Excellence for Climate Extremes (CE170100023), and by the Australian Bureau of Meteorology. Thanks are due to Alain Protat, chief scientist during the Australian leg of the YMC campaign, the Australian Marine National Facility, the RV Investigator crew, and the YMC science team for the soundings used in this study.

Data availability statement. The code written to generate and plot the solutions, and animated versions of key figures, are freely available online (Short 2023). The YMC sounding data is also freely available online (Protat and McRobert 2020a).

APPENDIX

A1. Parabolic Cylinder Functions

In this appendix we describe the functions $D_a(z)$ and $D_b(z)$. First note that parabolic cylinder functions can be expressed as the product of a "wave-like" exponential function, and a power series (e.g. Wünsche 2003), so that the solution to equation 41 can be written

$$\hat{\psi} = b_1 D_a(z) + b_2 D_b(z) \tag{A1}$$

$$= b_1 e^{-i\frac{Z(z)^2}{2}} U_{-\frac{1}{2}}((1+i)Z(z)) + b_2 e^{i\frac{Z(z)^2}{2}} U_{-\frac{1}{2}}((1-i)Z(z)), \tag{A2}$$

for constants $b_1, b_2 \in \mathbb{C}$, where

$$U_{-\frac{1}{2}}((1\pm i)Z(z)) = \sum_{k=0}^{\infty} \frac{(-1)^k \Gamma\left(k+\frac{1}{2}\right)}{\Gamma\left(\frac{2k+3}{4}\right) k!} e^{\pm ik\frac{\pi}{4}} Z(z)^k. \tag{A3}$$

Alternatively (Wünsche 2003),

$$\begin{aligned} U_{-\frac{1}{2}}((1\pm i)Z(z)) &= \frac{\sqrt{\pi}}{\Gamma\left(\frac{3}{4}\right)}{}_1F_1\left(\frac{1}{4};\frac{1}{2};\pm iZ(z)^2\right) - \frac{\sqrt{2\pi}}{\Gamma\left(\frac{1}{4}\right)}(1\pm i)Z(z){}_1F_1\left(\frac{3}{4};\frac{3}{2};\pm iZ(z)^2\right) \\ &= \sqrt{\frac{\pi Z(z)}{2}}\left[e^{\pm i\frac{Z(z)^2}{2}}J_{-\frac{1}{4}}\left(\frac{Z(z)^2}{2}\right) - e^{\pm i\left(\frac{Z(z)^2}{2}+\frac{\pi}{4}\right)}J_{\frac{1}{4}}\left(\frac{Z(z)^2}{2}\right)\right], \end{aligned} \tag{A4}$$

where ${}_1F_1$ is the confluent hypergeometric function of the first kind, which may be expressed using Bessel functions of the first kind $J_{\pm\frac{1}{4}}$ (Abramowitz and Stegun 1972), with additional simplifications as $Z(z)$ is real and non-negative. Thus

$$\mathrm{Re}\left(U_{-\frac{1}{2}}((1\pm i)Z)\right) = \sqrt{\frac{\pi Z}{2}}\left\{\cos\left(\frac{Z^2}{2}\right)J_{-\frac{1}{4}}\left(\frac{Z^2}{2}\right) - J_{\frac{1}{4}}\left(\frac{Z^2}{2}\right)\cos\left(\frac{\pi}{4}+\frac{Z^2}{2}\right)\right\} \tag{A5}$$

$$\mathrm{Im}\left(U_{-\frac{1}{2}}((1\pm i)Z)\right) = \pm\sqrt{\frac{\pi Z}{2}}\left\{\sin\left(\frac{Z^2}{2}\right)J_{-\frac{1}{4}}\left(\frac{Z^2}{2}\right) - J_{\frac{1}{4}}\left(\frac{Z^2}{2}\right)\sin\left(\frac{\pi}{4}+\frac{Z^2}{2}\right)\right\}, \tag{A6}$$

so that

$$\mathrm{Re}(U_{-\frac{1}{2}}((1+i)Z(z))) = \mathrm{Re}(U_{-\frac{1}{2}}((1-i)Z(z))), \tag{A7}$$

$$\mathrm{Im}(U_{-\frac{1}{2}}((1+i)Z(z))) = -\mathrm{Im}(U_{-\frac{1}{2}}((1-i)Z(z))), \tag{A8}$$

and hence

$$\hat{\psi} = b_1D_a(z) + b_2D_b(z) \tag{A9}$$

$$= b_1A(z)e^{-i\frac{Z(z)^2}{2}+i\theta(z)} + b_2A(z)e^{i\frac{Z(z)^2}{2}-i\theta(z)}, \tag{A10}$$

where $A(z)$ and $\theta(z)$ are real valued functions, corresponding to the amplitude and argument of the complex valued function $U_{-\frac{1}{2}}((1\pm i)Z(z))$ respectively. As a function of Z, $\theta(Z=0)=0$, which follows from equation A3, and remarkably, $\lim_{Z\to\infty}\theta(Z) = -\frac{\pi}{8}$, which follows from substituting the large asymptotic expressions for the Bessel functions in equations A5 and A6 (e.g. Whittaker and Watson 1996).

Plots of $A(z)$ and $\theta(z)$ are provided in the online supplement, and while difficult to prove formally, it is apparent that these functions do not oscillate for $z \in D_{\mathrm{TL}}$. Furthermore, in this

form the functions $D_a(z)$ and $D_b(z)$ bear a close resemblance to the first order Wentzel, Kramers and Brillouin (WKB) approximate solutions to equation 41, and thus the functions $D_a(z)e^{it}$ and $D_b(z)e^{-it}$ can be interpreted as modulated upward and downward propagating waves respectively; further details are provided in the online supplement. In the form of equation A10, algebra involving $D_a(z)$ and $D_b(z)$ is considerably simpler, and in their Bessel function forms, A and θ can be rapidly calculated to machine precision, simplifying numerical implementation.

A2. Transition Layer Expressions

As discussed in section 3, the transition-layer solution can be derived by separately solving for $G(z,z')$ for the subcases $z' \in D_1$, $z' \in D_{\mathrm{TL}}$ and $z' \in D_2$. Here we present the expressions for G associated with $\hat{\psi}_1$, the leftward propagating mode: the expressions associated with the rightward propagating mode $\hat{\psi}_2$ are analogous.

In the derivation for the $z' \in D_1$ case, which is included in the online supplement, the following expressions arise.

$$\alpha(z) = iZ(z)\frac{dZ(z)}{dz} - i\frac{d\theta}{dz} \tag{A11}$$

$$= \begin{cases} im(1+\mathcal{M}(z-\mathcal{H}_1)) - i\frac{d\theta}{dz} & \mathcal{N} > 1, \\ -im(1+\mathcal{M}(z-\mathcal{H}_1)) - i\frac{d\theta}{dz} & \mathcal{N} < 1, \end{cases} \tag{A12}$$

$$\beta = \frac{im\mathcal{N} + \alpha(\mathcal{H}_2) - \frac{A'(\mathcal{H}_2)}{A(\mathcal{H}_2)}}{2\alpha(\mathcal{H}_2)}, \tag{A13}$$

$$X = \frac{1}{2}\left[\frac{(1-\beta)D_a(\mathcal{H}_1)}{D_a(\mathcal{H}_2)} + \frac{\beta D_b(\mathcal{H}_1)}{D_b(\mathcal{H}_2)}\right], \tag{A14}$$

$$Y = \frac{1}{2im}\left\{\frac{(1-\beta)D_a(\mathcal{H}_1)}{D_a(\mathcal{H}_2)}\left[-\alpha(\mathcal{H}_1) + \frac{A'(\mathcal{H}_1)}{A(\mathcal{H}_1)}\right] + \frac{\beta D_b(\mathcal{H}_1)}{D_b(\mathcal{H}_2)}\left[\alpha(\mathcal{H}_1) + \frac{A'(\mathcal{H}_1)}{A(\mathcal{H}_1)}\right]\right\}, \tag{A15}$$

$$P = (X+Y)e^{im\mathcal{H}_1} + (X-Y)e^{-im\mathcal{H}_1}, \tag{A16}$$

where θ and A are defined in appendix A1, and A' denotes $\frac{dA}{dz}$. For $z' \in D_1$, G is then given by,

$$G = \begin{cases} -\frac{1}{mP}\left[(X-Y)e^{im(z'-\mathcal{H}_1)} + (X+Y)e^{-im(z'-\mathcal{H}_1)}\right]\sin(mz) & z \in D_1, z \le z', \quad \text{(A17a)} \\ -\frac{1}{mP}\sin(mz')\left[(X-Y)e^{im(z-\mathcal{H}_1)} + (X+Y)e^{-im(z-\mathcal{H}_1)}\right] & z \in D_1, z' < z, \quad \text{(A17b)} \\ -\frac{1}{mP}\left[\frac{(1-\beta)}{D_a(\mathcal{H}_2)}D_a(z) + \frac{\beta}{D_b(\mathcal{H}_2)}D_b(z)\right]\sin(mz') & z \in D_{\mathrm{TL}}, \quad \text{(A17c)} \\ -\frac{1}{mP}\sin(mz')e^{im\mathcal{N}(z-\mathcal{H}_2)} & z \in D_2, \quad \text{(A17d)} \end{cases}$$

These expressions are analogous to expressions 34a - 34c. The amplitudes $X-Y$ and $X+Y$ appear in place of $\frac{\mathcal{N}+1}{2}$ and $\frac{1-\mathcal{N}}{2}$ in equations 25 and 34a-34c, and approach these as $\mathcal{H}_2 \to \mathcal{H}_1$. The reflection and refraction coefficients are given by $r_1 = \left|\frac{X+Y}{X-Y}\right|$ and $r_2 = \left|\frac{1}{X-Y}\right|$ respectively.

When solving for G in the $z' \in D_{\mathrm{TL}}$ case, the following expressions arise.

$$\gamma = \frac{m\cos(m\mathcal{H}_1) + \sin(m\mathcal{H}_1)\left(-\frac{A'(\mathcal{H}_1)}{A(\mathcal{H}_1)} + \alpha(\mathcal{H}_1)\right)}{2\alpha(\mathcal{H}_1)} \quad \text{(A18)}$$

$$\mu = \gamma(1-\beta)D_b(\mathcal{H}_2)D_a(\mathcal{H}_1) - (\sin(m\mathcal{H}_1) - \gamma)\beta D_a(\mathcal{H}_2)D_b(H_1) \quad \text{(A19)}$$

$$U(z') = -\frac{D_a(\mathcal{H}_2)D_b(\mathcal{H}_1)D_a(\mathcal{H}_1)\beta}{2\mu\alpha(z')D_a(z')} - \frac{D_b(\mathcal{H}_2)D_b(\mathcal{H}_1)D_a(\mathcal{H}_1)(1-\beta)}{2\mu\alpha(z')D_b(z')} \quad \text{(A20)}$$

$$V(z') = -\frac{D_a(\mathcal{H}_1)D_b(\mathcal{H}_2)D_a(\mathcal{H}_2)\gamma}{2\mu\alpha(z')D_a(z')} - \frac{D_b(\mathcal{H}_1)D_b(\mathcal{H}_2)D_a(\mathcal{H}_2)\left(\sin(m\mathcal{H}_1) - \gamma\right)}{2\mu\alpha(z')D_b(z')} \quad \text{(A21)}$$

For $z' \in D_{\mathrm{TL}}$, G is given by

$$G = \begin{cases} U(z')\sin(mz) & z \in D_1, \quad \text{(A22a)} \\ U(z')\left[\frac{(\sin(m\mathcal{H}_1)-\gamma)}{D_a(\mathcal{H}_1)}D_a(z) + \frac{\gamma}{D_b(\mathcal{H}_1)}D_b(z)\right] & z \in D_{\mathrm{TL}}, z \le z', \quad \text{(A22b)} \\ V(z')\left[\frac{(1-\beta)}{D_a(\mathcal{H}_2)}D_a(z) + \frac{\beta}{D_b(\mathcal{H}_2)}D_b(z)\right] & z \in D_{\mathrm{TL}}, z' < z \quad \text{(A22c)} \\ V(z')e^{im\mathcal{N}(z-\mathcal{H}_2)} & z \in D_2. \quad \text{(A22d)} \end{cases}$$

These expressions describe the vertical response to a point forcing within the transition-layer D_{TL}, and have no direct analogue in the piecewise-constant solution. A vertically non-propagating wave, and a wave satisfying the radiation condition, are evident in D_1 and D_2 respectively.

Finally, when solving for G when $z' \in D_2$, the following expressions arise.

$$T = \frac{1}{2}\left[\frac{(\sin(m\mathcal{H}_1)-\gamma)\,D_a(\mathcal{H}_2)}{D_a(\mathcal{H}_1)} + \frac{\gamma D_b(\mathcal{H}_2)}{D_b(\mathcal{H}_1)}\right] \tag{A23}$$

$$S = \frac{1}{2im\mathcal{N}}\left\{\frac{(\sin(m\mathcal{H}_1)-\gamma)\,D_a(\mathcal{H}_2)}{D_a(\mathcal{H}_1)}\left[-\alpha(\mathcal{H}_2)+\frac{A'(\mathcal{H}_2)}{A(\mathcal{H}_2)}\right] + \frac{\gamma D_b(\mathcal{H}_2)}{D_b(\mathcal{H}_1)}\left[\alpha(\mathcal{H}_2)+\frac{A'(\mathcal{H}_2)}{A(\mathcal{H}_2)}\right]\right\} \tag{A24}$$

For $z' \in D_2$, G is then given by

$$G = \begin{cases} \frac{-1}{2im\mathcal{N}(S-T)} e^{im\mathcal{N}(z'-\mathcal{H}_2)} \sin(mz) & z \in D_1, \quad \text{(A25a)} \\ \frac{-1}{2im\mathcal{N}(S-T)} e^{im\mathcal{N}(z'-\mathcal{H}_2)} \left[\frac{(\sin(m\mathcal{H}_1)-\gamma)}{D_a(\mathcal{H}_1)} D_a(z) + \frac{\gamma}{D_b(\mathcal{H}_1)} D_b(z)\right] & z \in D_{\mathrm{TL}}, \quad \text{(A25b)} \\ \frac{-1}{2im\mathcal{N}(S-T)} e^{im\mathcal{N}(z'-\mathcal{H}_2)} \left[(S+T)e^{im\mathcal{N}(z-\mathcal{H}_2)} - (S-T)e^{-im\mathcal{N}(z-\mathcal{H}_2)}\right] & z \in D_2, z \le z' \quad \text{(A25c)} \\ \frac{-1}{2im\mathcal{N}(S-T)} \left[(S+T)e^{im\mathcal{N}(z'-\mathcal{H}_2)} - (S-T)e^{-im\mathcal{N}(z'-\mathcal{H}_2)}\right] e^{im\mathcal{N}(z-\mathcal{H}_2)} & z \in D_2, z' < z, \quad \text{(A25d)} \end{cases}$$

These expressions are analogous to expressions 36a - 36c. The amplitudes $S+T$ and $S-T = \overline{S+T}$ appear in place of R and $\overline{R}$, and approach these as $\mathcal{H}_2 \to \mathcal{H}_1$. The ducting coefficient is given by $r_3 = \left|\frac{1}{2i(S+T)}\right|$.

It is straightforward to show each of the above expressions for G approach their piecewise-constant forms as $\mathcal{H}_2 \to \mathcal{H}_1$, and those of the base solution of Rotunno (1983) as $\mathcal{N} \to 1$. Also, as $\mathcal{H}_2 - \mathcal{H}_1 \to \infty$, the functions $\frac{d\theta}{dz}$ and $\frac{dA}{dz}$ approach zero, and from the large asymptotic expressions for the Bessel functions in equations A5 and A6, we can show $\left|\frac{A(\mathcal{H}_2)}{A(\mathcal{H}_1)}\right|$ approaches $\sqrt{\mathcal{N}}$, from which the long limit expressions for the reflection, refraction and ducting coefficients follow.

Note that Bessel functions $J_{\pm\frac{1}{4}}\left(\frac{Z(z)^2}{2}\right)$ approximate their large asymptotic forms when $\frac{Z^2}{2} \gg \frac{3}{16}$ (Abramowitz and Stegun 1972), which requires $\min\left[\frac{m}{|\mathcal{M}|}, \frac{m\mathcal{N}^2}{|\mathcal{M}|}\right] \gg \frac{3}{8}$, from which follows inequalities 49 and 50. Analogously, approximate convergence to the short limit occurs when $\max\left[\frac{m}{|\mathcal{M}|}, \frac{m\mathcal{N}^2}{|\mathcal{M}|}\right] \ll 1$, from which follows inequalities 51 and 52.

One final limiting behaviour remains to be checked. Suppose that instead of $n(z)$ varying linearly over the transition-layer between 1 and $\mathcal{N}$, the transition-layer consists of $d \ge 2$ discontinuities in N, with a constant difference between subsequent values of $n(z)$, with the discontinuities equally spaced between $\mathcal{H}_1$ and $\mathcal{H}_2$. We would expect the solution in this case to approach that of the continuous linear transition-layer as $d \to \infty$. While difficult to prove in complete generality, in the

online supplement we illustrate this behaviour with examples. The wave modulation associated with $D_a(z)$ and $D_b(z)$ can thus be understood as the combined effect of many small reflections and refractions in the limit as the number of stability discontinuities becomes large.

References

Abramowitz, M., and I. Stegun, 1972: *Handbook of Mathematical Functions with Formulas, Graphs, and Mathematical Tables*. U.S. Department of Commerce, NIST.

Alexander, M. J., P. T. May, and J. H. Beres, 2004: Gravity waves generated by convection in the Darwin area during the Darwin Area Wave Experiment. *Journal of Geophysical Research: Atmospheres*, **109 (D20)**, https://doi.org/10.1029/2004JD004729.

Bergemann, M., C. Jakob, and T. P. Lane, 2015: Global detection and analysis of coastline-associated rainfall using an objective pattern recognition technique. *Journal of Climate*, **28 (18)**, 7225–7236, https://doi.org/10.1175/JCLI-D-15-0098.1.

Dacie, S., and Coauthors, 2019: A 1D RCE study of factors affecting the tropical tropopause layer and surface climate. *Journal of Climate*, **32 (20)**, 6769–6782, https://doi.org/10.1175/JCLI-D-18-0778.1.

Dalu, G. A., and R. A. Pielke, 1989: An analytical study of the sea breeze. *Journal of the Atmospheric Sciences*, **46 (12)**, 1815–1825, https://doi.org/10.1175/1520-0469(1989)046⟨1815:AASOTS⟩2.0.CO;2.

Das Gupta, A. J., A. S. V. Murthy, and R. S. Nanjundiah, 2015: A study of singularities in the inviscid linear theory of sea breezes. *International Journal of Advances in Engineering Sciences and Applied Mathematics*, **7 (1)**, 33–37, https://doi.org/10.1007/s12572-015-0129-y.

Drobinski, P., R. Rotunno, and T. Dubos, 2011: Linear theory of the sea breeze in a thermal wind. *Quarterly Journal of the Royal Meteorological Society*, **137 (659)**, 1602–1609, https://doi.org/10.1002/qj.847.

Du, Y., and R. Rotunno, 2015: Thermally driven diurnally periodic wind signals off the east coast of China. *Journal of the Atmospheric Sciences*, **72 (7)**, 2806–2821, https://doi.org/10.1175/JAS-D-14-0339.1.

Du, Y., and R. Rotunno, 2018: Diurnal cycle of rainfall and winds near the south coast of China. *Journal of the Atmospheric Sciences*, https://doi.org/10.1175/JAS-D-17-0397.1.

Du, Y., R. Rotunno, and F. Zhang, 2019: Impact of vertical wind shear on gravity wave propagation in the land–sea-breeze circulation at the equator. *Journal of the Atmospheric Sciences*, **76 (10)**, 3247–3265, https://doi.org/10.1175/JAS-D-19-0069.1.

Feng, S., Y. Fu, and Q. Xiao, 2012: Trends in the global tropopause thickness revealed by radiosondes. *Geophysical Research Letters*, **39 (20)**, https://doi.org/10.1029/2012GL053460.

Fueglistaler, S., A. Dessler, T. Dunkerton, I. Folkins, Q. Fu, and P. Mote, 2009: Tropical tropopause layer. *Reviews of Geophysics*, **47 (1)**, https://doi.org/10.1029/2008RG000267.

Gille, S., S. Smith, and N. Statom, 2005: Global observations of the land breeze. *Geophysical Research Letters*, **32 (5)**, https://doi.org/10.1029/2004GL022139.

Hankinson, M. C. N., M. J. Reeder, and T. P. Lane, 2014: Gravity waves generated by convection during TWP-ICE: I. Inertia-gravity waves. *Journal of Geophysical Research: Atmospheres*, **119 (9)**, 5269–5282, https://doi.org/10.1002/2013JD020724.

Hecht, J. H., S. Kovalam, P. T. May, G. Mills, R. A. Vincent, R. L. Walterscheid, and J. Woithe, 2004: Airglow imager observations of atmospheric gravity waves at Alice Springs and Adelaide, Australia during the Darwin Area Wave Experiment (DAWEX). *Journal of Geophysical Research: Atmospheres*, **109 (D20)**, https://doi.org/10.1029/2004JD004697.

Hu, S., and G. K. Vallis, 2019: Meridional structure and future changes of tropopause height and temperature. *Quarterly Journal of the Royal Meteorological Society*, **145 (723)**, 2698–2717, https://doi.org/10.1002/qj.3587.

Jiang, Q., 2012a: A linear theory of three-dimensional land-sea breezes. *Journal of the Atmospheric Sciences*, **69 (6)**, 1890–1909, https://doi.org/10.1175/JAS-D-11-0137.1.

Jiang, Q., 2012b: On offshore propagating diurnal waves. *Journal of the Atmospheric Sciences*, **69 (5)**, 1562–1581, https://doi.org/10.1175/JAS-D-11-0220.1.

Kilpatrick, T., S.-P. Xie, and T. Nasuno, 2017: Diurnal convection-wind coupling in the Bay of Bengal. *Journal of Geophysical Research: Atmospheres*, **122 (18)**, 9705–9720, https://doi.org/10.1002/2017JD027271.

Lane, T. P., 2021: Does lower-stratospheric shear influence the mesoscale organization of convection? *Geophysical Research Letters*, **48 (3)**, e2020GL091 025, https://doi.org/10.1029/2020GL091025, e2020GL091025 2020GL091025.

Li, Y., and J. Chao, 2016: An analytical solution for three-dimensional sea–land breeze. *Journal of the Atmospheric Sciences*, **73 (1)**, 41–54, https://doi.org/10.1175/JAS-D-14-0329.1.

Lin, P., D. Paynter, Y. Ming, and V. Ramaswamy, 2017: Changes of the tropical tropopause layer under global warming. *Journal of Climate*, **30 (4)**, 1245–1258, https://doi.org/10.1175/JCLI-D-16-0457.1.

Lindzen, R. S., and K.-K. Tung, 1976: Banded convective activity and ducted gravity waves. *Monthly Weather Review*, **104 (12)**, 1602–1617, https://doi.org/10.1175/1520-0493(1976)104⟨1602:BCAADG⟩2.0.CO;2.

Mapes, B. E., T. T. Warner, and M. Xu, 2003: Diurnal patterns of rainfall in northwestern South America. Part III: Diurnal gravity waves and nocturnal convection offshore. *Monthly Weather Review*, **131 (5)**, 830, https://doi.org/10.1175/1520-0493(2003)131⟨0830:DPORIN⟩2.0.CO;2.

Minobe, S., and S. Takebayashi, 2015: Diurnal precipitation and high cloud frequency variability over the Gulf Stream and over the Kuroshio. *Climate Dynamics*, **44 (7)**, 2079–2095, https://doi.org/10.1007/s00382-014-2245-y.

Mori, S., and Coauthors, 2004: Diurnal land–sea rainfall peak migration over Sumatera island, Indonesian Maritime Continent, observed by TRMM satellite and intensive rawinsonde soundings. *Monthly Weather Review*, **132 (8)**, 2021–2039, https://doi.org/10.1175/1520-0493(2004)132⟨2021:DLRPMO⟩2.0.CO;2.

Mowbray, D. E., and B. S. H. Rarity, 1967: A theoretical and experimental investigation of the phase configuration of internal waves of small amplitude in a density stratified liquid. *Journal of Fluid Mechanics*, **28 (1)**, 1–16, https://doi.org/10.1017/S0022112067001867.

Niino, H., 1987: The linear theory of land and sea breeze circulation. *Journal of the Meteorological Society of Japan. Ser. II*, **65 (6)**, 901–921, https://doi.org/10.2151/jmsj1965.65.6_901.

Ogura, Y., and N. A. Phillips, 1962: Scale analysis of deep and shallow convection in the atmosphere. *Journal of the Atmospheric Sciences*, **19 (2)**, 173–179, https://doi.org/10.1175/1520-0469(1962)019⟨0173:SAODAS⟩2.0.CO;2.

Pan, L. L., W. J. Randel, B. L. Gary, M. J. Mahoney, and E. J. Hintsa, 2004: Definitions and sharpness of the extratropical tropopause: A trace gas perspective. *Journal of Geophysical Research: Atmospheres*, **109 (D23)**, https://doi.org/10.1029/2004JD004982.

Pandya, R., D. Durran, and C. Bretherton, 1993: Comments on "thermally forced gravity waves in an atmosphere at rest". *Journal of Atmospheric Sciences*, **50 (24)**, 4097–4101, https://doi.org/10.1175/1520-0469(1993)050⟨4097:COFGWI⟩2.0.CO;2.

Pandya, R. E., D. R. Durran, and M. L. Weisman, 2000: The influence of convective thermal forcing on the three-dimensional circulation around squall lines. *Journal of the Atmospheric Sciences*, **57 (1)**, 29–45, https://doi.org/10.1175/1520-0469(2000)057⟨0029:TIOCTF⟩2.0.CO;2.

Protat, A., V. Louf, J. Soderholm, J. Brook, and W. Ponsonby, 2022: Three-way calibration checks using ground-based, ship-based, and spaceborne radars. *Atmospheric Measurement Techniques*, **15 (4)**, 915–926, https://doi.org/10.5194/amt-15-915-2022, URL https://amt.copernicus.org/articles/15/915/2022/.

Protat, A., and I. McRobert, 2020a: RV investigator in2019_v06 basta radar and radiosonde data. Commonwealth Scientific and Industrial Research Organisation, accessed 23/02/2023, https://doi.org/10.25919/5ef5a70ae2be9.

Protat, A., and I. McRobert, 2020b: Three-dimensional wind profiles using a stabilized shipborne cloud radar in wind profiler mode. *Atmospheric Measurement Techniques*, **13 (7)**, 3609–3620, https://doi.org/10.5194/amt-13-3609-2020.

Qian, T., C. C. Epifanio, and F. Zhang, 2009: Linear theory calculations for the sea breeze in a background wind: The equatorial case. *Journal of the Atmospheric Sciences*, **66 (6)**, 1749–1763, https://doi.org/10.1175/2008JAS2851.1.

Qian, T., C. C. Epifanio, and F. Zhang, 2012: Topographic effects on the tropical land and sea breeze. *Journal of the Atmospheric Sciences*, **69 (1)**, 130–149, https://doi.org/10.1175/JAS-D-11-011.1.

Robinson, F. J., S. C. Sherwood, and Y. Li, 2008: Resonant response of deep convection to surface hot spots. *Journal of the Atmospheric Sciences*, **65 (1)**, 276–286, https://doi.org/10.1175/2007JAS2398.1.

Rotunno, R., 1983: On the linear theory of the land and sea breeze. *Journal of the Atmospheric Sciences*, **40 (8)**, 1999–2009, https://doi.org/10.1175/1520-0469(1983)040⟨1999:OTLTOT⟩2.0.CO;2.

Schmidt, T., G. Beyerle, S. Heise, J. Wickert, and M. Rothacher, 2006: A climatology of multiple tropopauses derived from GPS radio occultations with CHAMP and SAC-C. *Geophysical Research Letters*, **33 (4)**, https://doi.org/10.1029/2005GL024600.

Short, E., 2023: rotunno83. Accessed 17/03/2023, https://github.com/eshort0401/rotunno83.

Sutherland, B. R., 2010: *Internal Gravity Waves*. Cambridge University Press, https://doi.org/10.1017/CBO9780511780318.

Vincent, C. L., and T. P. Lane, 2016: Evolution of the diurnal precipitation cycle with the passage of a Madden-Julian Oscillation event through the Maritime Continent. *Monthly Weather Review*, **144 (5)**, 1983–2005, https://doi.org/10.1175/MWR-D-15-0326.1.

Vincent, C. L., and T. P. Lane, 2018: Mesoscale variation in diabatic heating around Sumatra, and Its Modulation with the Madden–Julian Oscillation. *Monthly Weather Review*, **146 (8)**, 2599–2614, https://doi.org/10.1175/MWR-D-17-0392.1.

Vincent, R. A., A. MacKinnon, I. M. Reid, and M. J. Alexander, 2004: VHF profiler observations of winds and waves in the troposphere during the Darwin Area Wave Experiment (DAWEX). *Journal of Geophysical Research: Atmospheres*, **109 (D20)**, https://doi.org/10.1029/2004JD004714.

Whittaker, E. T., and G. N. Watson, 1996: *A Course of Modern Analysis*. 4th ed., Cambridge Mathematical Library, Cambridge University Press, https://doi.org/10.1017/CBO9780511608759.

Wünsche, A., 2003: Generalized Hermite polynomials associated with functions of parabolic cylinder. *Applied Mathematics and Computation*, **141 (1)**, 197–213, https://doi.org/10.1016/

S0096-3003(02)00333-8, advanced Special Functions and Related Topics in Differential Equations, Third Melfi Workshop, Proceedings of the Melfi School on Advanced Topics in Mathematics and Physics.

Yan, H., and R. Anthes, 1987: The effect of latitude on the sea breeze. *Monthly weather review*, **115 (5)**, 936–956, https://doi.org/10.1175/1520-0493(1987)115⟨0936:TEOLOT⟩2.0.CO;2.

Yang, G.-Y., and J. Slingo, 2001: The diurnal cycle in the tropics. *Monthly Weather Review*, **129 (4)**, 784–801, https://doi.org/10.1175/1520-0493(2001)129⟨0784:TDCITT⟩2.0.CO;2.

Yoneyama, K., and C. Zhang, 2020: Years of the Maritime Continent. *Geophysical Research Letters*, **47 (12)**, https://doi.org/10.1029/2020GL087182.